12-13-2019

Fabrication, Characterization and Application of Zinc Oxide and Zinc Magnesium Oxide Nanostructures

Abdiel Rivera
University of Connecticut - Storrs, abdiel.rivera@uconn.edu

ABSTRACT

Fabrication, Characterization and Application of Zinc Oxide and Zinc Magnesium Oxide Nanostructures

Abdiel Rivera, PhD

University of Connecticut, 2020

Zinc oxide is a wide bandgap semiconductor with relatively large exciton energy of 60 meV, and longitudinal optical phonon energy of 72 meV. ZnO can be grown in any nanostructure (nanoribbons, nanowires, nanorods, films, core-shell, among others), under any growth condition (metal-organic chemical vapor deposition (MOCVD), molecular beam epitaxial (MBE), hydrothermal, radio-frequency sputtering, sonochemical, etc) to be implemented in a variety of applications. For instance, by adding Mg to ZnO, the energy band separation increases and shift to a lower wavelength. Using ZnMgO, in the form of vertical nanowires, can improve the resolution of solar-blind UV-detectors. Nevertheless, the sol-solubility of ZnO – MgO phase diagram, exemplify the challenges to increase the Mg mole fraction without resulting in MgO mix phase.

In this study, the Mg mole fraction under MOCVD synthesis is pushed from 19% to 30%, without MgO phase, by adjusting the growth parameters. The highest Mg mole fraction yet, for nanowires, is validated using EDS on SEM and TEM, XRD and PL. During the characterization of the ZnMgO nanowires, it is observed that the lattice volume does not remain constant with the increment of Mg mole fraction as it has been, until now, assumed. Based on these observations and using experimental data, new stiffness coefficients are proposed.

Abdiel Rivera - University of Connecticut, 2020

Taking advantage of the very well developed ZnMgO vertically aligned nanowires, co-axial core-shell structures are grown using MOCVD and employed as a gas sensor. It is noted that the gas sensitivity of the ZnMgO/ZnO core-structures has a direct correlation with the Mg mole fraction at the core. It is also validated that the native defects, specifically, the doubly charged oxygen vacancy (V_o^{2+}) are responsible for the trapping and de-trapping of the gas molecules. In addition to vertically aligned nanowires, for the first time, purely ZnO horizontal nanowires in the absence of any assisting mechanism, have been grown on p-Si substrate. Typically, quasi-horizontal nanowires are grown by pre-treating the substrate using patterns, etching or catalyst. In this study it was found that a low concentration of zinc nitrate, when compare to hexamethylenetetramine needs to be maintained in the aqueous solution to preclude the growth of ZnO (002).

Fabrication, Characterization and Application of Zinc Oxide and Zing Magnesium Oxide Nanostructures

Abdiel Rivera

B.S., University of Turabo, Caguas, Puerto Rico, 2008

M.S., University of Connecticut, Storrs, CT, USA, 2011

A Dissertation

Submitted in Partial Fulfillment of the

Requirements for the Degree of

Doctor of Philosophy

at the

University of Connecticut

2020

APPROVAL PAGE

Doctor of Philosophy Dissertation

Fabrication, Characterization and Application of Zinc Oxide and Zinc Magnesium Oxide Nanostructures

Presented by

Abdiel Rivera, B.S., M.S.

Major Advisor _____

Mehdi Anwar

Associate Advisor _____

Helena Silva

Associate Advisor _____

Faquir Jain

Associate Advisor _____

Necmi Biyiki

University of Connecticut

2020

ACKNOWLEDGEMENT

I would like to express my deepest gratitude and appreciation to my major advisor, Dr. Mehdi Anwar, for his invaluable advice, mentorship, guidance, and encouragement during the last several years. This dissertation would not have been possible without his constant support, motivation, and availability to help me throughout the duration of my Ph.D. program.

I am grateful to my associate advisors, Dr. Helena Silva, Dr. Ali Gokirmak, Dr. Faquir Jain and Dr. Necmi Biyiki, for serving on my dissertation advisory committee as Associate Advisors. I would also like to acknowledge the financial support from University of Connecticut Graduate School Multicultural Scholarship Program (MSP) and U.S. Department of Education Graduate Assistance in Areas of National Need (GAANN).

I am especially grateful to my family for supporting me through all these years. I would like to express my gratitude to the two persons that gave me the first opportunity to do research and encouraged me to pursue a Ph.D. degree, Dr. Lee Aggison Jr. and Dr. Ruth Washington. Finally, I would like to thank my friends and fellow graduate students that have accompanied me during this journey and in one way or another helped to make this possible.

Table of Contents

List of Tables

List of Figures

Chapter 1

Introduction

ZnO has a direct energy band gap of 3.37 eV, a relatively large exciton energy of 60 meV, and longitudinal optical (LO) phonon energy of 72 meV, making it suitable for optoelectronic applications1 including quantum cascade lasers (QCLs), ultraviolet (UV) light-emitting diodes (LEDs), and UV detectors. ZnO nanowires (NWs) and nanorods (NRs) have been found to exhibit large spontaneous and strain-induced piezoelectric polarizations, enabling them to be harnessed for energy harvesting applications. In addition, the thermoelectric property of ZnO NWs has been utilized by fabricating nanoscale devices for energy scavenging. Furthermore, ZnO is chemically stable and biocompatible, making ZnO NW/NR-based devices suitable for biosensing applications. ZnO-based ternaries realized by the incorporation of Mg, Cd, Be, Co among others, allow bandgap engineering and a wide application platform. In particular, bandgap energy can be increased by increasing Mg mole fraction in $Zn_{1-x}Mg_xO$ crystals, making them suitable for development of solar blind detectors and ZnMgO/ZnO HEMT.

1.1 Literature Review - Growth Technique:

Pulse Laser Deposition (PLD)

Pulse laser deposition (PLD) is a method, as the name suggests, that it use a laser pulse to strike the material (targets) that will be deposited on the substrate. These targets are prepared by milling the powders (the source, i.e. ZnO, MgO, CdO, etc) together, pressed

and sintered at high temperatures for a long time [1]. When the laser hit the target(s) it generates a plasma that it gets transfer to the substrate using a carrier gas, typically Argon. In addition to Argon, Oxygen is also flowed through the chamber to oxidize the sample. The substrate is heated up as a mechanism to control the nucleation density. The growth of the ZnO nanowire, particularly the growth rate is controlled by the duration and frequency of the laser pulse. A. Shkurmanov et al. [2] presented at the 30th Eurosensors Conference in 2016 that in order to control the lateral and vertical growth rate: i) the seed layer must be formed of a nuclei pyramids, ii) high laser pulses, which in turn is directly proportional to the amount of Zn delivered to the sample, prioritize the vertical growth over the lateral growth leading to the growth of thin NWs (thickness ~100nm, length ~2.3µm for ~24kpulses).

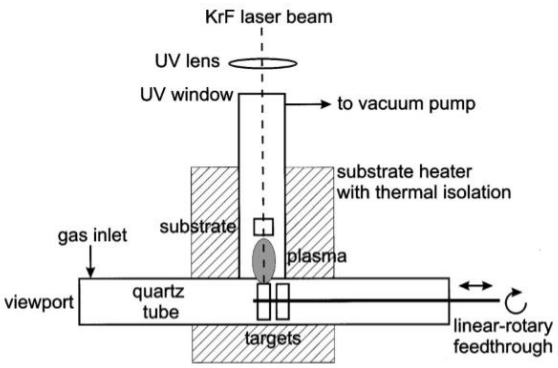

FIG. 1. Scheme of high-pressure PLD chamber for nanoheterostructures.

Fig. 1.1: Scheme of high-pressure PLD chamber for nanoheterostructures. [3]

Other parameters that can influence the morphology, density, and quality of the nanowires are the laser energy density, the distance between the target and the substrate, the gas flow rates and the pressure of the chamber. For gold assisted growth the oxygen partial pressure, as pointed out by Zhang et al. [4], influenced the morphological quality of the nanowires, scilicet, at high partial pressure the nucleation of ZnO seem to be originated

from other facets not the preferential site of the liquid-alloy-ZnO interface, turning into random morphologies. Figure 1.2 shows the SEM of ZnO NWs under two different oxygen partial pressure, 2 Torr and 0.2 Torr.

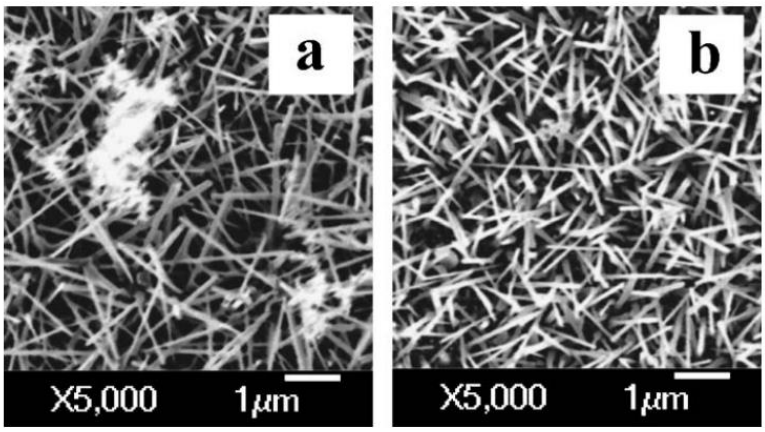

Fig. 1.2: SEM image of ZnO nanowires under two different oxygen partial pressure [4].

Molecular Beam Epitaxy (MBE)

Molecular beam epitaxy (MBE) is a fabrication technique mostly used to grow thin film under high or ultra-high vacuum. The high vacuum must be maintained evenly along the chamber to guarantee the uniformity of the structure. The MBE chamber does not use a carrier gas which should minimize the defects associated with gases like N_2. The targets are heated up independently using quasi-Knudsen effusion cells (observed in figure 1.3) or electron beam evaporators, until it begins to sublime. The gases will condense on the surface of the substrate where will react with each other. The flow rate of the gases is controlled by small orifices at the targets using shutters that regulates the flux of the molecular beams. One of the biggest advantages of the MBE systems is that the quality of the structure can be monitored in-situ with reflection high energy electron diffraction spectroscopy (RHEED). However, most of the reported growth of ZnO nanowires using

MBE uses gold as a catalyst which can incorporate unintentional defects by leaving remnants of gold all over the sample, in particular, on the tip of the nanowire.

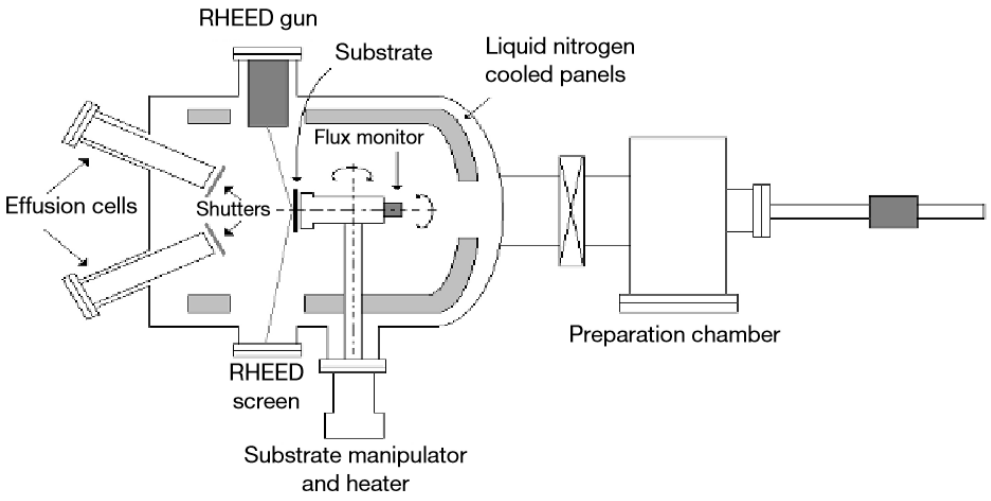

Fig. 1.3: Schematic diagram of an MBE growth chamber [5].

For example, Isakov et al. [6] studied the effects of the morphology of the Au layer over the ZnO nanowires by varying the diameter and separation between gold nanoparticles. The nanowires were only grown in a temperature starting around 700°C and not to exceed 800°C as the natural SiO_2 evaporates bringing Au in contact with Si. Isakov projected that the optimal growth temperature should be around 850°C as the wall of the nanowires becomes parallel with temperature and at the same time that the density of the nanowires increases by activating more gold nanodots. As a way to increase further the growth temperature, Isakov suggested a buffer layer of ZnO grown prior to depositing the gold layer, for 10 min at 750°C. The SEM of the NWs grown at 850°C using the buffer layer is compared to those grown on Au at 750 and 800°C in figure 1.4 showing an increased of about 100 times more nanowires per area. The Zn beam-equivalent pressure was also found to be limited in the range of $1x10^{-7}$ to $5x10^{-7}$ Torr.

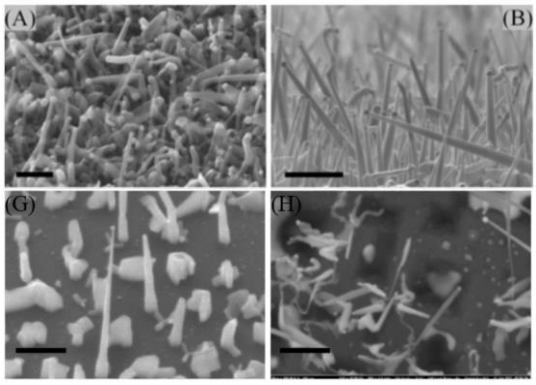

Fig. 1.4: (A) and (B) SEM images of the samples grown on Si with Au-thin film as a catalyst at A) 45° view, B) 90° view, (H) are grown with colloidal gold as a catalyst at 750°C, (G) with EBL-patterned grown at 800°C [6].

DC/Radio Frequency (RF) Sputtering

Radio frequency (RF) sputtering, seen in figure 1.5, is not commonly used to growth ZnO nanowires, however, is one of the most common and inexpensive methods to deposit nanostructures ZnO films or seed layer at room temperature. The substrate is placed in a chamber under vacuum while the target (ZnO) is energized by very high voltage (upward 10^{12} V). An inert gas is inserted into the chamber that will be ionized through the RF waves. Once the ions make contact with the target material, the radio waves pull out the atoms into the surface of the substrate. Under RF sputtering the properties of the nanostructures are mostly controlled by the seed layer rather than RF power, pressure and gas flow rate [7]. The only documentation of ZnO nanowires grown using RF sputtering was published in 2003 by W.-T. Chiou et al. [8] and claimed the achievement was done by inducing additional strain over the surface by using a layer of copper. However, the nanowires were polycrystalline which was then improved, according to Chiou, with the addition of oxygen (O_2/Ar = 0.3) during the growth of the nanowires resulting in a single crystal. Figure 1.6

shows the progression of the nanowires upon growth duration, prior the growth, after 5 min and 30 min of deposition, respectively.

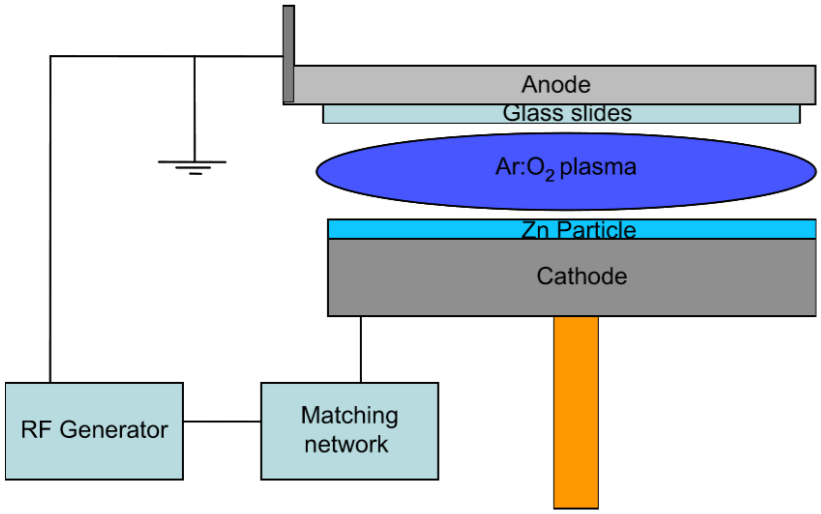

Fig. 1.5: Schematic drawing of the RF sputtering system [9].

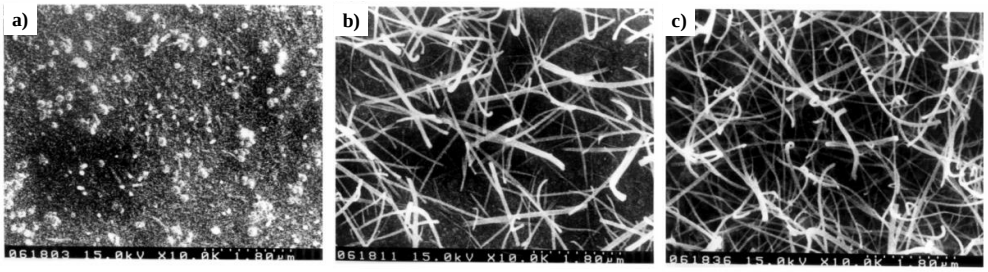

Fig. 1.6: SEM of ZnO nanowires grown at: a) initial growth, b) 5 min deposition and c) 30min deposition [8].

A more typical application for RF sputtering is to form core-shell structures by using ZnO NWs grown under other technique (i.e., MOCVD) and coat it with a thin layer. This is the case for J.P. Kar et al. [10] who grew a thin layer of ZnMgO on top of ZnO NWs previously grown using MOCVD. The challenge of this technique is to minimize the diffusion of the Mg into the ZnO layer as it is known that film grown using RF sputtering

requires high annealing temperatures. Kar annealed the ZnMgO film at 900°C for 1 min in nitrogen ambient using rapid thermal annealing treatment (RTA) in a way to reduce the diffusion of Mg and altering the size and shape of the nanostructures. Similar to the work done by J.P. Kar, H.W. Kim et al. [11] coated ZnO nanowires previously grown using CVD with aluminum doped ZnO film to form a p-n junction and to protect the ZnO NWs from oxidation.

Hydrothermal Synthesis

Hydrothermal synthesis is a solution phase synthesis carried out in an aqueous solution. For this process, the sample is placed upside down in an aqueous solution with some sort of zinc compound and a buffer to control the chemical reaction. Typically, methenamine (HMTA) is used to provides the hydroxyl ions to react with Zn^{2+} ions to form ZnO. The chemical reaction is summarized below. Then, the bottle with the sample is placed in a water bath at temperatures in the range of 60 to 95°C for 6 to 24hrs depending upon the desired properties of the nanowires/nanorods. Like in the MOCVD, the duration of the growth impacts the dimensions of the nanostructure while the orientation is determined by the seed layer.

In the hydrothermal method, the decomposition of the precursors $Zn(NO_3)_2 + 6H_2O$, HMTA, and DI water forms formaldehyde, ammonium, and hydroxide ($C_6H_{12}N_4 + H_2O \rightarrow 6HCHO + 4NH_4 + 4OH$). HMTA acts as a source of OH to drive the precipitation reaction. Hydroxide ions are released as the HMTA decomposes and controls the acidity of the solution by negating the effect of hydrogen ions. pH effects on the growth of ZnO have been noted by Ashford et al. [12] Zinc ions originating from the zinc nitrate are combined

with the hydroxide to form zinc oxide and water (Zn_2 + 2OH -> ZnO + H_2O). The concentration of Zn ions in the solution during the hydrothermal process is limited and decreases with increasing growth time.

Hydrothermal synthesis has been used to grow ZnO nanorods in a variety of substrates, p-Si(100), u-GaN/Sapphire and SiO_2/p-Si. As described by Ji et al. [13] the thickness and orientation of the seed layer influence the orientation of the nanostructure as thicker layer minimized the effect of defects and strain developed by lattice mismatch.

Although hydrothermal synthesis is a low-temperature process that can be used to growth ZnO nanostructures at a low cost, it has the disadvantage that the amount of Zn_2^+ ions decrease with growth time. The degree of supersaturation influences whether the growth of NWs (or NRs) continues along the vertical axis or if secondary growth from laterally oriented faceted ZnO ([0101]) occurs [14]. A low NH_4^+/Zn_2^+ ratio promotes the precipitation of ZnO resulting in high-density nucleation. Conversely, a high NH_4^+/Zn_2^+ ratio causes dissolution of ZnO and suppresses nucleation.

Sonochemical Synthesis

The sonochemical synthesis follows the same chemistry as hydrothermal, but it uses the extra energy of the ultrasound wave to increase the growth rate. The sonochemistry consists of gas bubbles generated by ultrasound collating against each other. Suslick et al. [15] explained that there are three regions which temperature varies from T > 5000K inside of the collapsing bubble, T~1900K at the interface of the bubble with the liquid and ambient temperature for the rest of the solution. It is in that intermediated state that X.L. Hu in 2004 [16] synthesized “unsuspended” ZnO nanowires using zinc nitrate and HMTA,

the same compounds described previously under hydrothermal growth. Hu concluded that the length of the nanowires would be dictated by the duration of the growth while the diameter (thickness) would vary upon HMTA/Zn^{2+}. In 2008, a professor from the Department of Chemical Engineering in a university in South Korea, Prof. S.-H. Jeong [17] reported vertically aligned ZnO nanorods arrays on various substrates using a 50W transducer @ 20kHz, as seen in Figure 1.7. For his work, the sonochemical process resulted in a growth rate of 500nm/hr in contrast to 40nm/hr using hydrothermal, at least 10 times faster.

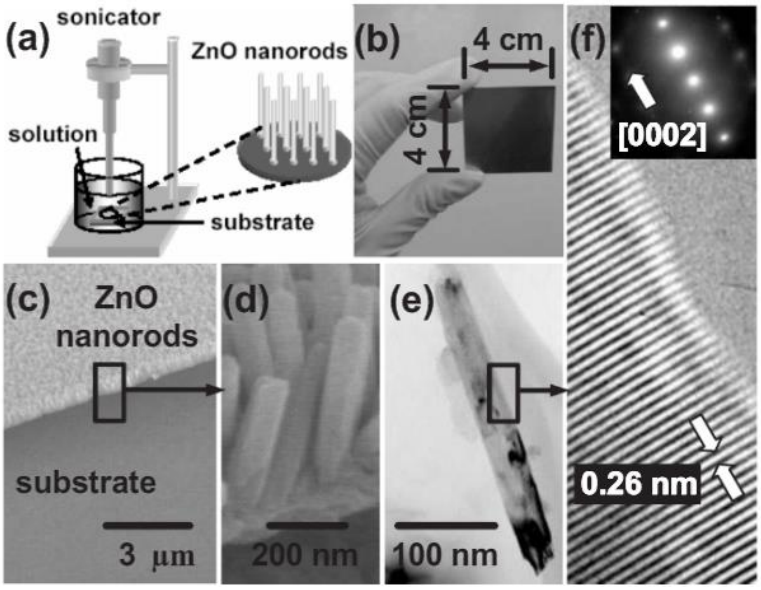

Fig. 1.7: a) Schematic illustration of a sonochemical route to vertically ZnO nanorods on various substrate. B) 4 cm x 4 cm Zn sheet after 1h of ZnO growth. C) A tilt view SEM image of ZnO nanorods arrays grown on a Zn sheet. d) A magnified view of oriented ZnO nanorods with length of 50 to 150 nm, and diameter of 300 to 900 nm. e) TEM and f) an HRTEM of a single ZnO nanorods detached from the Zn sheet. [17]

Metal Organic Chemical Vapor Deposition (MOCVD)

The MOCVD uses metal-organics as the precursors for the deposition. The metal organics are storage in their liquid form, but by adjusting the pressure and the temperature

in the bubbler, the vapor phase is taken using a carrier gas (i.e., N_2, Ar, H_2, etc.). These gases are introduced into the chamber where will react with the oxidizer gas on the surface of the substrate. The chemical composition of the growth is controlled by the relative ratio of the mixed gases. The substrate is kept in a heated-up furnace which temperature and pressure are controlled to guarantee the uniformity of the growth. MOCVD is a much simpler process and carries a faster growth rate (around 10times [18] as compared to MBE.

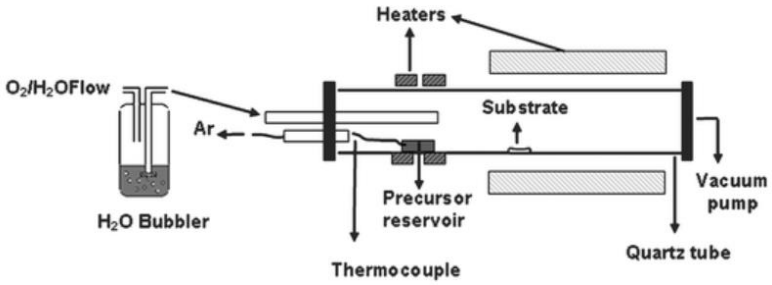

Fig. 1.8: MOCVD hot-wall reactor scheme [19]

MOCVD has many advantages, but it lacks in-situ characterization and tailoring the right chemistry to achieves ZnO NWs can be quite challenging. Not only the formation of ZnO NWs varies upon the employed metal-organic (i.e., DEZn (Diethelzinc), Me_2Zn (dimethylzinc), Et_2Zn (diethyl zinc), among others) but also upon carrier gas (i.e., Ar_2, N_2) and oxygen source (i.e., O_2, N_2O). The thermodynamics of the gas-phase reactions need to be adjusted to minimize premature reaction, as the gases most react at the surface of the substrate. A study made by K. Black et al. [20] concluded that like in the case of the precursor Et_2Zn, Me_2Zn(THF), for the same flow rates of precursor and oxygen source, it has a narrow temperature window that will result in nanowires. Figure 1.9 shows the SEM of the ZnO deposited on Si(111) varying the temperature from 475 to 525°C while keeping the Zn/O ratio constant. Also, as it will be described further in the thesis, the lattice

mismatch that carry any substrates, impacts the orientation, thickness and lengths of the nanowires/nanorods.

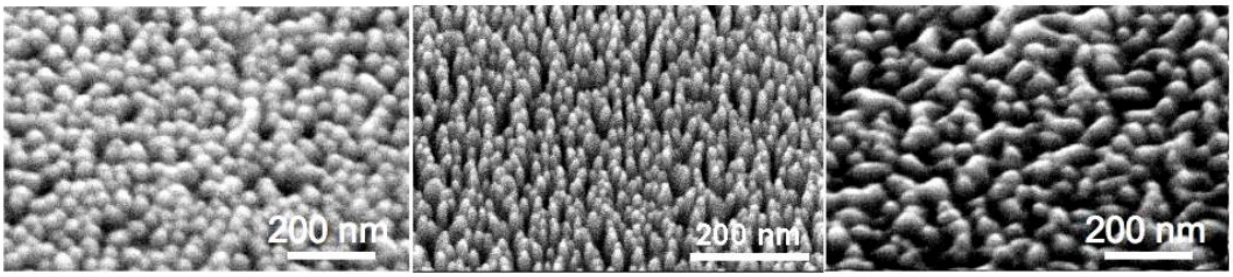

Fig. 1.9: SEM of ZNO deposited at 475°C (left), 500°C (middle) and 525°C (right) [20]

1.2 Objectives:

In this work, the main focus the growth, characterization and fabrication of ZnO and ZnMgO based devices providing the physics and the governing mechanism responsible of the intrinsic characteristic of ZnO. Special attention is given to ZnMgO NWs as limited work has been done and it has been rarely reported a single phase ZnMgO NWs with large Mg mole fraction without exhibiting characteristics of MgO mixed phase. The following is addressed in this study:

(i) Achieves the highest Mg mole fraction under MOCVD synthesis on ZnMgO nanowires without MgO mix phase. The crystal structure upon Mg mole fraction is explain and correlate to the strain and lattice constants.

(ii) Based on the observations that the lattice volume does not remain constant with the increment of Mg mole fraction as it has been and using experimental data, new stiffness coefficients are proposed.

(iii) Growth of the first horizontal nanowires on a substrate without pre-treating the surface of the substrate, the help of blocking layers or photoresist.

(iv) ZnO thin film is grown on p-Silicon substrate with hall electron mobility of 531 $cm^2/V.s$, currently the highest reported at room temperature is 440 $cm^2/V.s$.

(v) Explain the effect of Mg in ZnMgO/ZnO core-shell structure used as gas sensor and correlated to photoluminescence spectrum.

References:

1. M. Lorenz, E.M. Kaidashev, H. von Wenckstern, V. Riede, C. Bundesmann, et. al. ,Solid State Electronics 47 (2003) 2205-2209
2. A. Shkurmanov, C. Sturm, H. Hochmuth, M. Grundmann, Procedia Engineering 168 (2016) 1156 – 1159
3. M. Lorenza, E. M. Kaidashev, A. Rahm, Th. Nobis, J. Lenzner, et. al. Appl. Phys. Lett. 86, 143113 (2005)
4. Y. Zhang, R.E. Russo, and S.S. Mao, Appl. Phys. Lett. 87, 133115 (2005)
5. P. N. Prasad, Nanophotonics, John Wiley & Sons, Hoboken, New Jersey, 2004 (page 179)
6. I. Isakov, M, Panfilova, M.J. Sourribes, and P.A. Warburton, Phys. Status Solidi C 10, No. 10, 1308–1313 (2013)
7. J. Song, S. Lim, J. Phys. Chem. C 2007, 111, 596-600
8. W.-T. Chiou, W.-Y. Wu, J.-M. Ting, Diamond and Related Materials, 12, Issues 10–11, (2003) 1841
9. N. Ekem, S. Korkmaz, S. Pat, M.Z. Balbag, E.N. Cetin, M. Ozmumcu, International Journal of Hydrogen Energy, Volume 34, Issue 12, (2009) 5218

10. J.P. Kar, M.C. Jeong, W.K. Lee, J.M. Myoung, Materials Science and Engineering: B, Volume 147, Issue 1, (2008), 74-78,
11. H.W. Kim, M.A. Kebede, H. S. Kim, Current Applied Physics, Volume 10, Issue 1, (2010) 60
12. M.N.R. Ashfold, R.P. Doherty, N.G. Ndifor-Angwafor, D.J. Riley, Ye Sun, Thin Solid Films 515, 8679–8683 (2007)
13. L.-W. Ji, S.-M. Peng, J.-S. Wu, W.-S. Shih, C.-Z. Wu, I.-T. Tang, Journal of Physics and Chemistry of Solids, Volume 70, Issue 10, (2009) 1359
14. H.Q. Le, S.J. Chua, Y.W. Koh, K.P. Loh, E.A. Fitzgerald, Journal of Crystal Growth, Volume 293, Issue 1, (2006) 36
15. K.S. Suslick, Science 23 Mar 1990:Vol. 247, Issue 4949, pp. 1439-1445
16. X.-L. Hu, Y.-J. Zhu, S.-W. Wang, Materials Chemistry and Physics, Volume 88, Issues 2–3, (2004) 421
17. S.-H. Jung, E. Oh, K.-H. Lee, W. Park, S.-H. Jeong, Adv. Mater. 2007, 19, 749–753
18. P. N. Prasad, Nanophotonics (John Wiley & Sons, Hoboken, New Jersey, 2004)
19. R.L. Nigro, R.G. Toro, G. Malandrino and I.L. Fragala. J. Mater. Chem., 2005,15, 2328-2337
20. K. Black, A.C. Jones, I. Alexandrou, P.N. Heys, and P.R Chalker, Nanotechnology 21 (2010) 045701

Chapter 2

Growth of ZnO Nanowires

In this chapter, the growth and optimization process of the ZnO seed layer used for the nanowires (NWs) and nanorods (NRs) is described. Then, a comparison of ZnO NWs and NRs grown using metalorganic chemical vapor deposition (MOCVD) and hydrothermal synthesis, respectively, on *p*-Si (100), GaN/sapphire, and SiO_2 substrates is presented. Finally, the morphology and crystal structure of the ZnO NWs and NRs are analyzed under scanning electron microscope (SEM), x-ray diffraction (XRD) and photoluminescence (PL).

2.1 ZnO Seed Layer:

2.1.1 Growth of ZnO Seed Layer

ZnO thin films were deposited on p-Si and GaN substrates using FirstNano EasyTube 3000 MOCVD system at a constant temperature and pressure of 300° C and 70 Torr, respectively. Diethylzinc (DEZn) and N_2O were used as the zinc and oxygen precursors and nitrogen was used as the carrier gas. The growth was carried out for 20 mins maintaining a steady flow of 50 SCCM and 35 SCCM of DEZn and N_2O, respectively. After deposition of the thin film, the samples were annealed at 500 – 750° C under N_2 ambient.

2.1.2 Annealing

The ZnO thin films grown on p-Si and GaN substrate were annealed at 500 – 750° C under N_2 ambient. The scanning electron microscope (SEM) images shown in figure 2.1

and 2.2, shows the surface of the film corresponding to p-Si and GaN substrate, respectively, under different annealing conditions. Thermal annealing at 500 to 600° C, for p-Si, resulted in a smoother film with smaller RMS roughness. As the temperature increased, > 700° C, large grains with grain sizes between 35 to 155 nm were observed. Meanwhile, the film grown on GaN substrate showed better morphology in general. Figure 2.2 shows the surface of the film for annealing temperature as grown, 500, 600, 700 and 750° C. The smoothness of the surface for ZnO film grown on GaN could be related to the small lattice mismatch between ZnO and GaN, about 2% (compressive strain), in contrast with 40% of tensile strain between ZnO and p-Si.

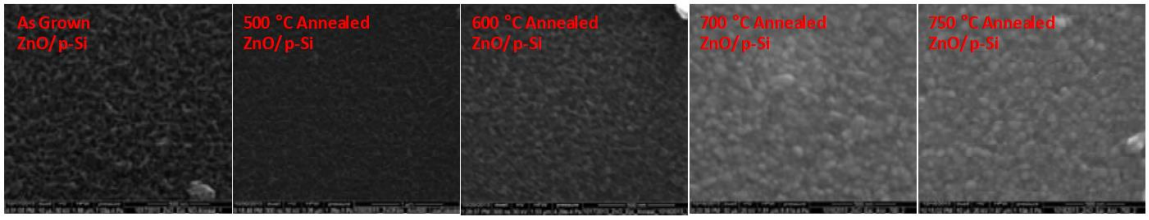

Fig. 2.1: SEM of ZnO thin film grown on p-Si substrate as a function of annealing temperature (as grown, 500, 600, 700 and 750° C).

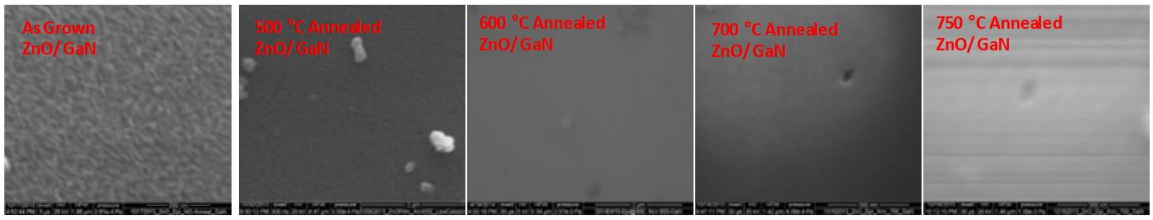

Fig. 2.2: SEM of ZnO thin film grown on GaN substrate as a function of annealing temperature (as grown, 500, 600, 700 and 750° C).

In order to investigate the origin of the granular textures, the samples were annealed and cooled at a slower rate of 2.5 °C/min which is twice as slower than the regular annealing condition used in this study. SEM images of the thin film annealed at different rates and temperatures are shown in Figure 2.3. The slower annealing/ cooling rate did not show any

observable difference in the grain size of ZnO thin films on different substrates compared to their faster annealed counterparts. This suggests that the observed granular surface texture at higher annealing temperature is not a direct result of the thermal coefficient mismatch. Rather, at high annealing temperatures the grain boundaries migrate and the adjacent grains coalesce, independent of the annealing/ cooling ramp [1]

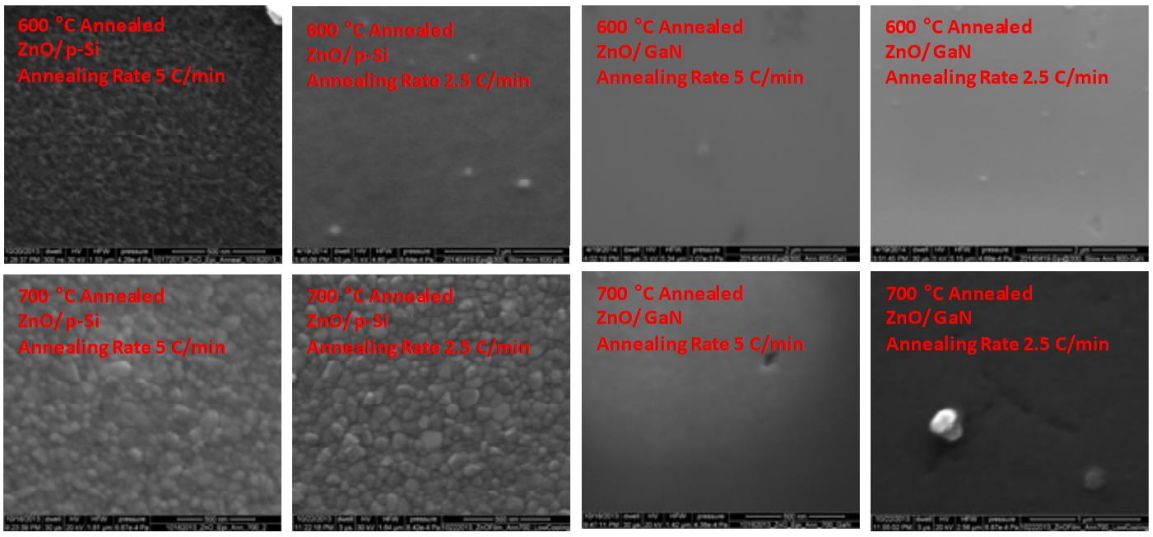

Fig. 2.3: Slow Vs. fast annealing/cooling ramp for ZnO thin film grown on p-Si and GaN substrates, respectively

To have a better understanding of the effect of the annealing temperature over the crystal structure, x-ray diffraction (XRD) measurements were taken. The as grown samples shows diffraction peaks corresponding to ZnO (100), (002), (102) and (110). As illustrated in figure 2.4, the ZnO film became more single crystalline with (002) orientation, when annealed at 600°C. It is important to point out that, although the cooling rate did not impact the morphology of the surface it intensified the diffraction peak of ZnO (002) suggesting a predominant orientation of the film.

Table 1 summarizes the crystalline quality of ZnO thin films grown on p-Si substrates

and annealed at different temperatures. The c-lattice constant is observed to decrease with increased annealing temperature which is in agreement with the observations made by other researchers [2-4]. Comparison of the full width at half maximum (FWHM) of the (002) peak suggests that the crystalline quality becomes better with higher temperature annealing and a slower anneal/ cooling ramp increases the film quality to a higher degree. For an example, the 700 °C slow annealed sample has a 56% smaller FWHM than the as-grown film.

Table 2.1: Summary of crystalline quality of ZnO thin film on p-Si substrates annealed at different temperatures.

	As-Grown	500 °C	600 °C	700 °C Slow	700 °C Fast
c-lattice (Å)	5.1921	5.1906	5.1820	5.1870	5.1891
a-lattice (Å)	3.2430	3.2430	3.2406	3.1792	3.2417
Misfit Strain	67.47%	67.47%	67.59%	70.83%	67.53%
FWHM (deg)	0.2225	0.1279	0.1280	0.09695	0.1239

2.2 Growth of ZnO NWs and NRs:

2.2.1 Metalorganic Chemical Vapor Deposition:

ZnO NWs were grown utilizing a First Nano EasyTube 3000 MOCVD at a constant pressure of 70 Torr. Diethylzinc (DEZn) was used as the Zn source, N_2O as the oxygen source, and N_2 as the carrier gas. Prior to growth, the samples were ultrasonically cleaned in acetone and methanol for 5 minutes each, rinsed with deionized (DI) water, and then dried in air in a laboratory oven. Initially, a ZnO thin film epilayer was grown as detailed in section 2.1. The epilayer was then annealed at 625ºC in a N_2 atmosphere. The NWs were grown at 625˚C for 20 minutes with DEZn and N_2O flow rates of 20 standard cubic centimeter (sccm) and 50 sccm, respectively.

Dumont et. al. [5] have suggested the occurrence of homolytic fission in the decomposition of DEZn, resulting in the formation of the hydrocarbons ethylene and ethane. Thiandoume et al. [6] reported the decomposition of DEZn versus temperature, observing a total dissipation at 360˚C which limits the minimum MOCVD growth temperature for the growth of ZnO NW. The lowest growth temperature reported using MOCVD is 200ºC involving the growth of ZnO thin films using DEZn and O_2 as the zinc and oxygen sources, respectively [7]. The use of N_2O as the oxygen source in the growth process may reduce premature oxidation of DEZn [8].

2.2.2 Hydrothermal:

The low temperature hydrothermal growth was performed in two steps. Initially, 90 mg of zinc acetate and 120 mg of potassium hydroxide were dissolved in 50 ml of methanol and then constantly stirred for 5 minutes at 60ºC. Using the zinc acetate solution as a seed layer, the samples were then spin coated. The epilayer was grown by immersing the samples in an aqueous $Zn(NO_3)_2$ solution of 0.1 M and 0.1 M of hexamethylenetetramine (HMTA) at 90ºC in a laboratory oven for 1 hour [9]. Finally, NR growth was accomplished in a water bath at 70˚C using an equi-aqueous solution of 25 mM $Zn(NO_3)_2$ and HMTA for 3-7 hours [10].

2.3 Characterization of ZnO NWs and NRs:

Figures 2.4 (a)-(c) shows scanning electron microscope (SEM) images of ZnO NWs grown using MOCVD on p-Si, GaN/sapphire, and SiO_2/p-Si substrates. The diameters and approximate lengths of the NWs varied from 90 – 150 nm and 1 – 2 μm on the p-Si

substrate, 20 – 40 nm and 0.7 – 1.0 μm on GaN, and 70 – 90 nm and 1 – 2 μm on SiO_2/p-Si, respectively. The dimensions of the NWs along with those for the NRs grown using the hydrothermal method are summarized in Table 2.2. The orientation of the nanowires varied from being perpendicular to the basal plane in the case of GaN substrates, tilted 60 – 80 degrees toward the c-axis for p-Si substrates, and randomly oriented for SiO_2 substrates. The small lattice mismatch between GaN and ZnO (1.8%) promoted the growth of ZnO NWs oriented along the c-axis [11]. Also, use of the ZnO thin film as a seed layer may have reduced the lattice mismatch and could result in vertically aligned NWs for other substrates such as Si with larger lattice mismatch [12]. In order to explore the stability of the NWs at different temperatures, SEM images were captured by increasing the temperature up to 800ºC in 100ºC increments. The morphology of the NWs remained unchanged after being exposed up to a temperature of 800ºC for 1 hour.

Table 2.2: Summary of dimensions and crystal quality of the NWs and NRs grown using MOCVD and hydrothermal process.

Dimensions and crystal structure	**p-Si(001)**		**GaN/sapphire(001)**		**SiO_2/p-Si(001)**	
	NW-MOCVD	**NR-Hydrother.**	**NW-MOCVD**	**NR-Hydrother.**	**NW-MOCVD**	**NR-Hydrother.**
Diameter (nm)	**90 - 150**	**200 - 300**	**20 - 40**	**200 - 350**	**70 - 90**	**200 - 350**
Length (μm)	**1 - 2**	**0.7 - 0.9**	**0.7 - 1.0**	**~ 1**	**1 - 2**	**~ 1**
ZnO (002) (2θ)°	**34.4798**	**34.4868**	**34.5784**	**34.51**	**34.3808**	**34.5**
c-lattice const. (Å)	**5.1982**	**5.1971**	**5.1838**	**5.1942**	**5.2127**	**5.19**
c-lattice strain (%)	**0.11**	**0.13**	**0.39**	**0.19**	**0.17**	**0.28**
FWHM (θ)	**0.0498**	**0.0591**	**0.0497**	**0.052**	**0.0588**	**0.0776**
FWHM (arcsec)	**179**	**213**	**178**	**187**	**212**	**279**

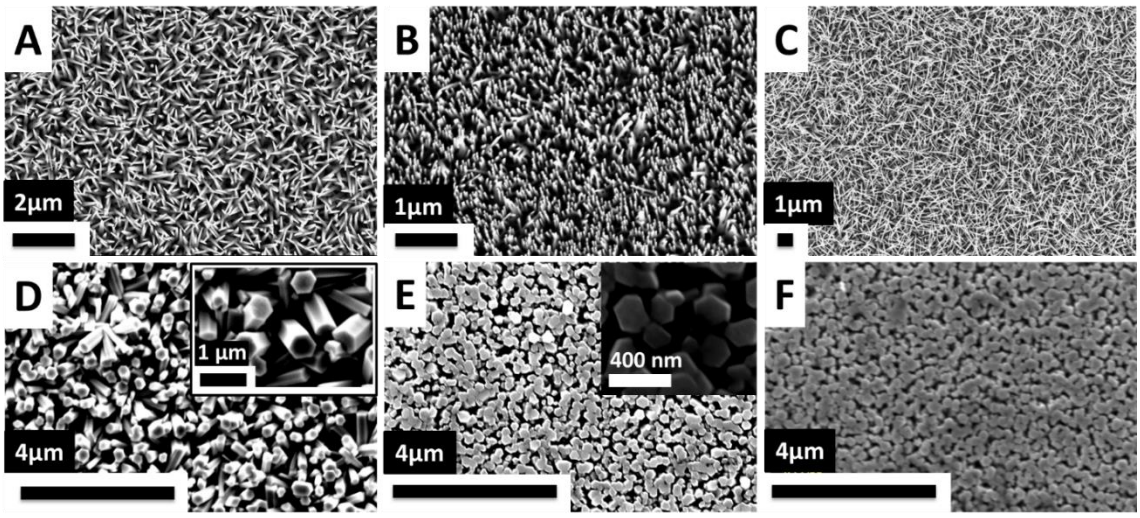

Fig. 2.4: SEM of ZnO NWs grown using MOCVD on (a) p-Si (100), (b) GaN/sapphire, and (c) SiO_2/p-Si. SEM of ZnO NRs grown using hydrothermal synthesis on (d) p-Si (100), (e) GaN/sapphire, and (f) SiO_2/p-Si.

Figures 2.4(d)-(f) show SEM images of ZnO NRs grown on p-Si, GaN/sapphire, and SiO2/p-Si substrates using the hydrothermal process. The NRs had hexagonal shapes and were mostly oriented along the (002) plane. The NRs grown on p-Si [Figure 2.4(d)] had diameters varying between 200 – 300 nm, with approximate lengths between 0.7 – 0.9 µm. Secondary nucleations were observed, where the tips of NRs functioned as the seed layer. In the hydrothermal method, the decomposition of the precursors Zn(NO3)2 + 6H2O, HMTA and DI water, forms formaldehyde, ammonium, and hydroxide (C6H12N4 + H2O ↔ 6HCHO + 4NH4 + 4OH). HMTA acts as a source of OH to drive the precipitation reaction. Hydroxide ions are released as the HMTA decomposes and controls the acidity of the solution by negating the effect of hydrogen ions. pH effects on the growth of the ZnO have been noted by Ashford et al. [13]. Zinc ions originating from the zinc nitrate are combined with the hydroxide to form zinc oxide and water (Zn2 + 2OH ↔ ZnO + H2O).

The concentration of Zn ions in the solution during the hydrothermal process is limited and decreases with increasing growth time.

The secondary nucleations observed in the inset of Figure 2.4(d) may be controlled by varying growth time and replacing the solution with a new solution during the growth process. As explained by Le et al. [14], the degree of supersaturation influences whether the growth of NWs (or NRs in this case) continues in the vertical axis or if secondary growth from laterally oriented faceted ZnO ([0101]) occurs. A low NH4+/Zn2+ ratio promotes the precipitation of ZnO resulting in high density nucleation. Conversely, a high NH4+/Zn2+ ratio causes the dissolution of ZnO and suppresses nucleation. To assure continuous growth of vertically aligned NRs, a fresh supply of reagent was needed. In the case of MOCVD NW synthesis, the precursor quantity was controlled during the growth to significantly reduce the probability of secondary nucleations.

Figures 2.4(e) and (f) show vertically aligned NRs grown on GaN and SiO2 substrates, respectively. The NRs had similar dimensions, with diameters that varied between 200 – 350 nm and approximately 1 μm in length. The energy diffraction spectroscopy (EDS) results shown in Figure 2.5 confirms that both the NWs and NRs exhibit clean surfaces without any trace of metal residue, which may be attributed to the growth being performed in the absence of metal catalysts.

A Bruker D-8 Advance X-ray diffractometer with a wavelength $\lambda = 1.5406$ Å corresponding to the Cu Kα line was used to investigate the crystal structure of grown NWs. Figure 3 shows the XRD pattern for the ZnO NWs grown on p-Si (black line), GaN (red) and SiO2 (blue) substrates using MOCVD. The inset of Figure 3 shows dominant peaks related to ZnO (002). For ZnO grown on p-Si and SiO2 substrates using MOCVD,

the peak at 34º (2θ) incorporated the overlapping of ZnO NWs (002) and ZnO thin film (002). In the case of the GaN/sapphire substrate, an additional diffraction peak associated with GaN was present. These peaks were resolved by using a Lorentzian fit, using Equation 2.1, a peak resulting from a combination of multiple peaks due to diverse crystal planes and/or materials may be decomposed to identify the constituent peaks providing the maximum and the full-width at half-maximum (FWHM) for each of the peaks.

$$y = y_0 + 2\frac{A}{\pi}\frac{w}{4(x - x_c)^2 + w^2} \tag{2.1}$$

Here y is the X-ray intensity, y_0 is the intensity offset, A is the area, w is the width and xc is the center peak angle. ZnO NWs oriented along the (002) direction had a maximum intensity at 34.4798º (2θ) and a full-width at half maximum (FWHM) of 0.0498° (θ) (179 arcsec) for p-Si, 34.5784º (2θ) and a FWHM of 0.0497(θ) (178 arcsec) for GaN, and 34.3808º (2θ) and a FWHM of 0.0588 (θ) (212 arcsec) for SiO_2. Lee et al. reported, for similar MOCVD growth conditions, FWHMs of 11.57º (41652 arcsec) and 0.053º (190.8 arcsec) for Si (100) and GaN/sapphire (001) substrates, respectively [15].

The c-lattice constants for the NWs grown using MOCVD were estimated to be 5.1982 Å, 5.1838 Å and 5.2127 Å for p-Si, GaN and SiO2, respectively, using Equation 2.2 [16]:

$$sin^2\theta = \frac{\lambda^2}{4}\left[\frac{4}{3}\left(\frac{h^2 + hk + k^2}{a^2}\right) + \frac{l^2}{c^2}\right] \tag{2.2}$$

where θ corresponds to the angle of diffraction, λ is the x-ray wavelength (1.5406 Å), and (h, k, l) are the Miller indices. The c-lattice constant reflected out-of-plane strains of 0.11%, 0.39% and 0.17% for p-Si, GaN and SiO_2, respectively, compared with unstrained ZnO (5.204 Å). Strain was estimated using : $\epsilon_\perp = (c_{grown} - c_{unstrained}) / c_{unstrained}$, where *c* is the c-lattice constant for ZnO. Figure 2.6 shows the strain associated with the c-lattice constant of the ZnO NWs for various MOCVD grown NW diameter ranges. The strain of

the c-lattice constant of the NW is increasing with decreasing NW diameter, which is consistent with the observations reported by Tsao et al. [17]. This observation suggests that the strain induced in the c-lattice constant by the effect of the substrate over the lattice mismatch between the substrate and the seed layer may alter the lateral and vertical growth rate, along with the alignment of the NWs.

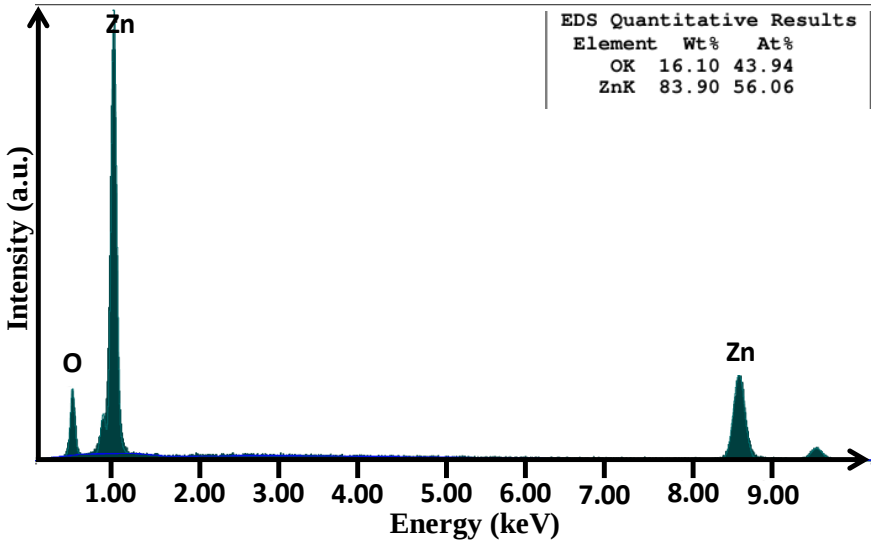

Fig. 2.5: Energy dispersive spectroscopy (EDS) of ZnO NWs grown on p-Si (100) using MOCVD, showing zinc and oxygen as the only two elements present in the structure.

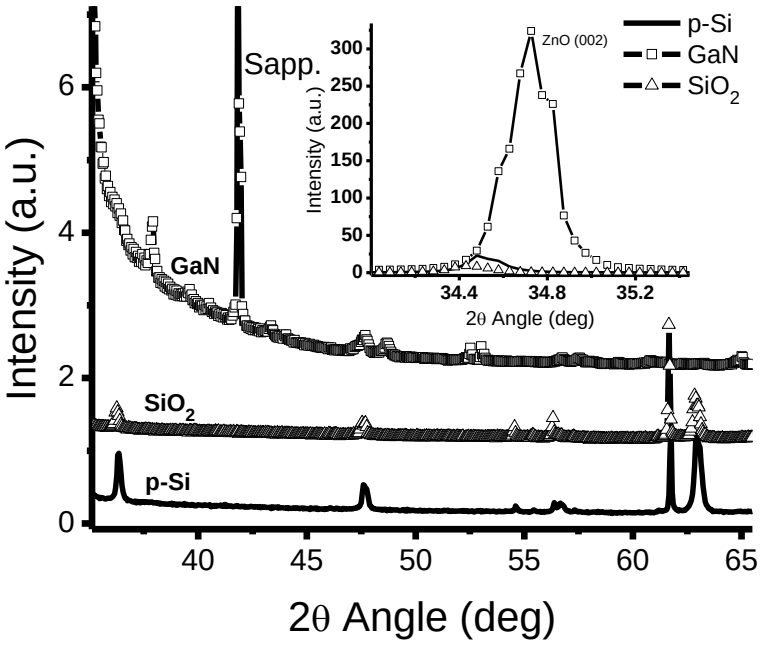

Fig. 2.6: XRD of ZnO NWs grown using MOCVD on p-Si (solid), GaN/sapphire (square) and SiO_2 (triangle). The inset shows the ZnO peak associated with ZnO oriented along (002) and GaN

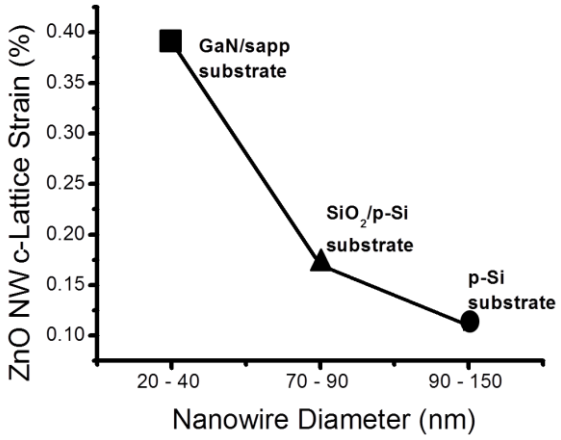

Fig. 2.7: Strain on the c-lattice constant of ZnO NWs versus diameter of NWs on GaN/sapphire (square), SiO_2/p-Si (triangle) and p-Si substrates (circle). The NWs were grown using MOCVD.

Figure 2.8 shows the XRD for ZnO NRs grown on p-Si, GaN, and SiO_2 substrates using the hydrothermal process. Compared to the samples grown using MOCVD, the peak intensities associated with ZnO along (002) were weaker, with a maximum at 34.4868º (2θ) and a FWHM of 0.0591 (θ) (213 arcsec) for p-Si, 34.510º (2θ) and a FWHM of 0.052 (θ) (187 arcsec) for GaN, and 34.50º (2θ) and a FWHM of 0.0776 (θ) (279 arcsec) for SiO2; the XRD results for the NRs and NWs are summarized in Table 2.2. The FWHM of the samples grown using MOCVD were smaller in comparison to the FWHM of the NRs grown on the same substrates using the hydrothermal process, which could indicate higher crystal quality. The c-lattice constants of the NRs grown using hydrothermal were estimated to be 5.1971 Å, 5.1942 Å and 5.1900 Å, reflecting a strain of approximately 0.13%, 0.19% and 0.28% for p-Si, GaN and SiO2, respectively. Additional shallow diffraction peaks were observed related to ZnO (100, 101, 102, 103, 200 and 110) and the corresponding substrates. The growth method for the ZnO epilayer used as the seed layer for the NRs does not necessarily provide uniformity, which could contribute to the randomness reflected in Figure 2.4(d). Alternatively, the ZnO seed layer could be grown on MOCVD prior to the growth of ZnO NRs using hydrothermal synthesis. Fragala et al. reported the growth of ZnO NRs by chemical bath deposition at 70ºC on a ZnO seed layer grown on MOCVD with the growth temperature varied over the 300 - 600ºC range and deposition time in the 10 - 60 minutes range [18]. The discontinuous film structure grown at 300ºC resulted in slanted and geometrically not well defined ZnO NRs, while geometrically defined grains grown in the 400 - 600˚C temperature range resulted in hexagonally shaped NRs with homogenous distribution, which were vertically aligned for growth temperatures above 500˚C.

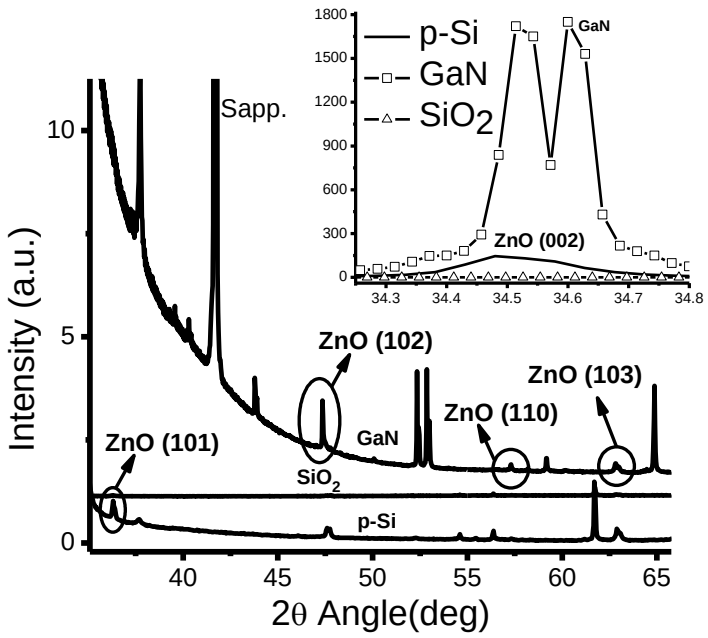

Fig. 2.8: XRD of ZnO NRs grown using hydrothermal synthesis on p-Si, GaN/sapphire and SiO_2. The inset shows the ZnO peak associated with ZnO oriented along 0002 and GaN (square), SiO_2 (triangle) and p-Si (solid). Shallow diffraction peaks associated with ZnO oriented along (101), (102), (110) and (103) are observed.

Figure 2.9 shows the PL spectra for ZnO nanowires grown on p-Si, GaN, and SiO_2 substrates. The PL was performed at room temperature using a Xenon light source centered at a wavelength of 280 nm. Single peaks located at 380 nm having a FWHM of 14.6932 nm and at 378 nm having a FWHM of 15 nm were observed for p-Si and SiO_2 substrates, respectively. These peaks corresponded to the recombination of excitons through an exciton–exciton collision process [19]. No apparent defects related to Zn or O vacancies were observed, which can be attributed to the confinement of defects at the ZnO thin film/substrate interface. Room temperature PL of ZnO NWs has been reported with excitation in the visible light spectrum (425 nm $\leq \lambda \leq$ 600 nm) regardless of the substrate [20-23]. For ZnO NWs grown on GaN using MOCVD, a predominant peak was located at

378 nm with a FWHM of 18.18 nm. The high stress of ZnO NWs grown on GaN, observed in Figure 2.6, can contribute to the broadening of the peak in comparison to p-Si and SiO_2, for the same growth method. A shallow peak was identified at 480 nm that upon decomposition using a Lorentzian fit resulted in observed peaks at 474 nm and 490 nm, which correlated to oxygen interstitial and oxygen vacancies, respectively [24].

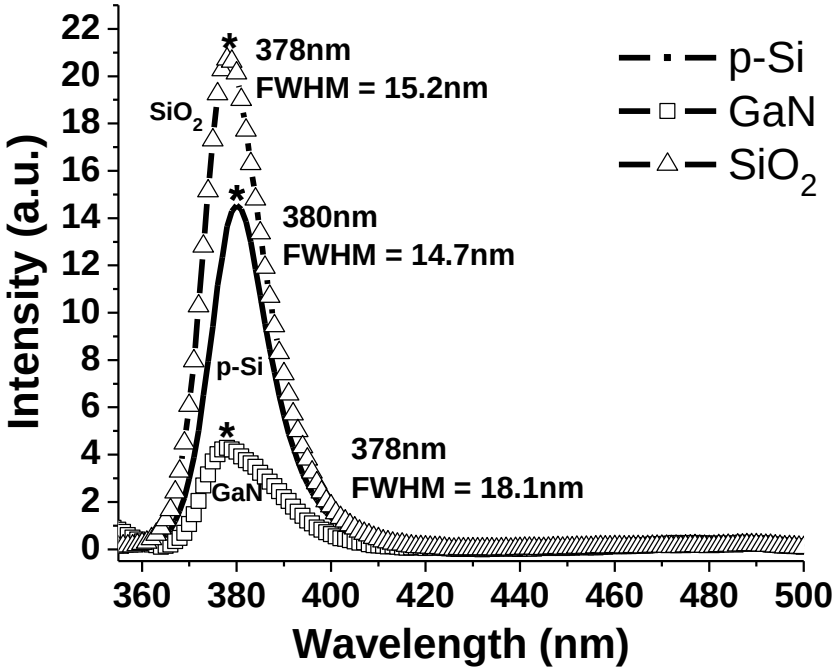

Fig. 2.9: PL of ZnO NWs grown using MOCVD on p-Si (100) (solid) with a single peak at 380 nm, GaN (square) with a stronger peak at 378 and SiO_2 (triangle) with a single peak at 378. Peaks are associated with exciton to exciton recombination.

2.4 Conclusions

In this chapter, the optimal growth conditions for the ZnO seed layer was developed. ZnO NWs and NRs were grown on p-Si (100), GaN, and SiO_2 substrates using both MOCVD and hydrothermal synthesis. The study characterization focus on the physical, crystal and optical properties of the nanowires/nanords. Based on the results obtained from the present study, the following conclusions can be made:

- Least surface roughness of the ZnO/p-Si thin films was obtained when annealed at 500-600 °C window. GaN substrates obtain better morphology of ZnO thin films than p-Si substrates due to a smaller lattice mismatch.
- The NWs had larger length-to-diameter ratios in comparison with the NRs. In addition, the MOCVD-grown NWs exhibited a clean surface in the absence of secondary nucleations, while some of the NRs grown on p-Si using the hydrothermal method overlapped with each other and showed secondary NRs nucleated from the tips of the primary
- As observed in SEM images and confirmed by XRD, the only truly vertically aligned growth using MOCVD was achieved for the NWs grown on GaN, in contrast to the NRs grown using hydrothermal synthesis which were mostly perpendicular to the surface regardless of the substrate.
- For NRs grown using hydrothermal synthesis, the orientation appeared to be related to the seed layer condition instead.
- The NWs demonstrated higher crystal quality than the NRs based on the XRD data, as the FWHMs of the XRD peak corresponding to ZnO (002) were 0.0498°, 0.0497°, and 0.0588° θ, in contrast with the NR FWHMs of 0.0591°,0.052°,and 0.0776° θ for p-Si, GaN/sapphire, and SiO2/p-Si substrates, respectively.
- Photoluminescence of the NWs grown on p-Si and SiO2 showed a single absorption peak associated with exciton– exciton recombination, while ZnO NWs grown on GaN/sapphire also had defects attributed to oxygen interstitials and oxygen vacancies.

References:

1. Y. Lin, J. Xie, H. Wang, Y. Li, C. Chavez, S. Lee, S. Foltyn, S. Crooker, A. Burrell and T. McCleskey, Thin Solid Films, vol. 492, pp. 101-104, 2005
2. V. Gupta and A. Mansingh, J. Appl. Phys., vol. 80, pp. 1063-1073, 1996
3. M. Puchert, P. Timbrell and R. Lamb, Journal of Vacuum Science & Technology A, vol. 14, pp. 2220- 2230, 1996.
4. Y. Lee, S. Hu, W. Water, K. Tiong, Z. Feng, Y. Chen, J. Huang, J. Lee, C. Huang and J. Shen, *J Lumin,* vol. 129, pp. 148-152, 2009
5. H. Dumont, A. Marbeuf, J.E. Bouree, and O. Gorochov, J. Mater. Chem. 2, 923 (1992).
6. C. Thiandoume, V. Sallet, R. Triboulet, and O. Gorochov, J. Cryst. Growth 311, 1411–1415 (2009).
7. B.P. Zhang, K. Wakatsuki, N.T. Binh, N. Usami, and Y. Segawa, Thin Solid Films 449, 12–19 (2004).
8. C.K. Lau, S.K. Tiku, and K.M. Lakin, J. Electrochem. Soc. 127, 1845 (1980).
9. D. Chu, T. Hamada, K. Kato, and Y. Masuda, Phys. Status Solidi A 206, 718–723 (2009).
10. P. Shimpi, P.X. Gao, D.G. Goberman, and Y. Ding, Nanotechnology 20, 125608 (2009).
11. C.H. Chen, S.J. Chang, S.P. Chang, M.J. Li, and I.C. Chen, et al., Appl. Phys. Lett. 95, 223101 (2009).
12. D.C. Kim, B.H. Kong, H.K. Cho, D.J. Park, and J.Y. Lee, Nanotechnology 18, 015603 (2007).

13. M.N.R. Ashfold, R.P. Doherty, N.G. Ndifor-Angwafor, D.J. Riley, and Y. Sun, Thin Solid Films 515, 8679–8683 (2007).
14. H.Q. Le, S.J. Chua, Y.W. Koh, K.P. Loh, and E.A. Fitzgerald, J. Cryst. Growth 293, 36–42 (2006).
15. D.J. Lee, J.Y. Park, Y.S. Yun, S. Hong, J.H. Moon, and B.T. Lee, et al., J. Cryst. Growth 276, 458 (2005).
16. B.D. Cullity, Elements of X-Ray Diffraction. Addison-Wesley Metallurgy Series (1956), p. 310.
17. F.C. Tsao, J.Y. Chen, C.H. Kuo, G.C. Chi, and C.J. Pan, Appl. Phys. Lett. 92, 203110 (2008).
18. M.E. Fragala, Y. Aleeva, and G. Malandrino, Thin Solid Films 519, 7694–7701 (2011).
19. B. Ha, H. Ham, and C.J. Lee, J. Phys. Chem. Solids 69, 2453–2456 (2008).
20. W. Lee, M.C. Jeong, and J.M. Myoung, Acta Mater. 52, 3949–3957 (2004).
21. J.H. Zeng, Y.L. Yu, Y.F. Wang, and T.J. Lou, Acta Mater. 57, 1813 (2009).
22. J.B. Baxter and E.S. Aydil, J. Electrochem. Soc. 156, H52– H58 (2009).
23. B. Ha, H. Ham, and C.J. Lee, J. Phys. Chem. Solids 69, 2453–2456 (2008).
24. A.B. Djurisic, A.M.C. Ng, and X.Y. Chen, Prog. Quant. Electron. 34, 191–259 (2010).

Chapter 3

Structural and Optical Properties of High Magnesium wurzite-ZnMgO Nanowires

This chapter presents wurzite-$Zn_{1-x}Mg_xO$ nanowires (NWs) grown using metalorganic chemical vapor deposition (MOCVD) technique with the highest Mg mole fraction of 0.29. The enhancement of the solubility limits, as reported, is accomplished by varying different growth parameters such as growth temperature, chamber pressure, growth duration, flow rates of the precursors, and smart use of the seed layer that also functions as buffer layers. The physical structures of the NWs are shown to remains invariant with increasing Mg incorporation while the diameters and lengths vary in the range 40-180nm and 0.5-1.5μm, respectively. XRD, PL and hall measurements are used to describe the effect of the Mg mole fraction into ZnMgO nanowires.

3.1 Growth of ZnMgO Nanowires

ZnMgO NWs were grown using a First Nano EasyTube 3000 MOCVD with a horizontal 3" furnace. Growth of $Zn_{1-x}Mg_xO$ NWs preceded an epitaxial layer of ZnO film on p-Si (100) substrates as described in section 2.1. The MOCVD growth used diethyl zinc (DEZn) (SAFC Hitech CAS:557-20-0) as the Zn precursor, N_2O as the oxygen source, and N_2 as the carrier gas. ZnO growth using MOCVD requires that the reaction of the metal organics take place on the surface of the substrate. N_2O was used rather than pure O_2 as oxygen source to prevent any pre-reaction with DEZn in the gas phase [1-2]. The epitaxial layer acts as (a) the seed for the growth of $Zn_{1-x}Mg_xO$ NWs and (b) a buffer absorbing the

strain resulting from large lattice mismatch of ~40% between Si-substrate and ZnO. After the growth of the ZnO seed layer the chamber pressure is dropped to 4 Torrs while the temperature is increased to 650˚C during growth of NWs on the ZnO buffer layer. Bis(cyclopentadienyl)Mg (Cp2Mg) (SAFC Hitech CAS:1284-72-6) is introduced in the chamber in the gas phase and serves as the Mg source. Different flow rates that resulted in a controllable Mg mole fraction are listed in Table 3.1. Mg incorporation is significantly increased when the nanowire growth is followed by a 10 min diffusion/drive-in step with a CP_2Mg/DEZn ratio of 200 and Mg drive-in at 900°C. Mg needs to be energetically activated, otherwise, the electrical/optical properties of Mg remains dormant. Mg activation is also commonly used for Mg-GaN grown using MOCVD. Mg activation is typically accomplished by annealing the samples at high temperatures (> 700˚C) that dissociates Mg-N-H complexes [3].

Table 3.1: $Zn_{1-x}Mg_xO$ NWs growth conditions. Details of growth for ZnO nanowires can be found in section 2.2-2.3.

x	DEZn	Cp_2Mg	N_2O	Duration (min)	Activation
0	20	0	285	60	N/A
0.04	10	150	500	60	900°C (10 min)
0.09	10	150	500	60	900°C (30 min)
0.19	10	200	500	60	900°C (10 min)
0.29	10	200	500	60 + 10 (drive in)	900°C (10 min)

3.2 Method

The crystal structures of the NWs were investigated using Quanta FEG 250 Scanning Electron Microscope (SEM) and Bruker D-8 Advance X-ray diffractometer (XRD) with a wavelength $\lambda = 1.5406$Å corresponding to the CuKα line. PL spectra of the Zn1-xMgxO samples ($x < 0.19$) were measured by exciting the samples with a Melles Griot Series 56,

HeCd laser with λ = 325nm and power of 18mW. For Zn0.71Mg0.29O NWs, room temperature PL was measured by using a 200 W - HgXe lamp in a built-in Newport housing and a bandpass filter at 239nm with 10nm bandwidth. The spectra were dispersed by a Horiba Jobin Yvon iHR 550 spectrometer and detected by a Si detector. The Hall mobility was measured at room temperature using Van Der Pauw geometry, with 6451 G magnet and a standard DC measurement set-up. Indium dots were soldered on to the corners of the sample using a home-built Indium soldering station that served as contact electrodes. The contacts were approximately 0.5mm x 0.5mm.

3.3 Results and Discussion

Figure 3.1-(a-e) show $Zn_{1-x}Mg_xO$ NWs grown using MOCVD with Mg mole fractions of x = 0, 0.04, 0.09, 0.19 and 0.29. All the samples showed an even distribution of NWs in a 0.5cm^2 area, attributed to the high quality of the ZnO epitaxial film used as seed layer. The ZnO seed layer (shown in figure 4-c) had c-lattice constant of 5.2Å and FWHM of 0.0332° (θ) (119.52 arcsec) suggesting superior quality than those reported by other authors, for example FWHM of 8100 arcsec reported by Jeong *et al.* [4] and 1080 arcsec reported by Yu *et al.* [5]. The growth mechanism can be seen of Stranski-Krastanov (SK) type where it starts as a layer-by-layer growth (ZnO buffer layer) but after a critical thickness is reached it becomes a three-dimensional (3D) growth (ZnMgO nanowires). The transition from SK to 3D type growth as observed in this work is obtained by adjusting the reactor temperature, from 300 to 625°C and by adjusting the metal organic flow rates as indicated in the experimental section, thereby, eliminating possibilities of parasitic ZnMgO film over-growth. In some instances where thicker diameter and shorter length NWs were

observed, the growth may be attributed to Wolmer-Weber growth mechanism where ZnMgO islands are grown on top the ZnO film.

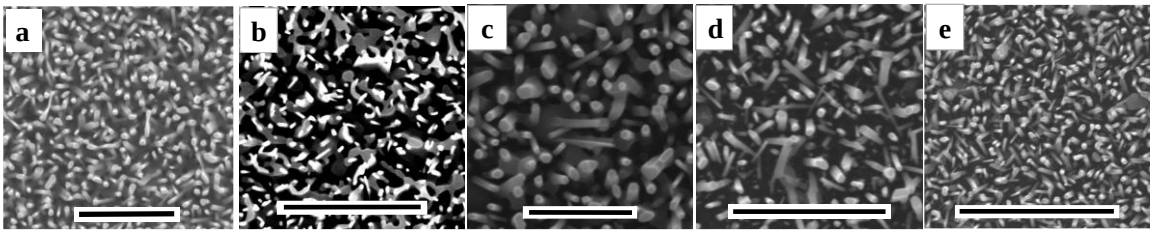

Fig. 3.1: SEM image of a Zn1-xMgxO NWs grown using MOCVD. (a) NWs with 0% Mg, 2µm scale bar (b) NWs with 4% Mg, 2µm scale bar (c) NWs with 9% Mg, 1µm scale bar. (d) NWs with 19% Mg, 2µm scale bar. (e) NWs with 29% Mg, 2µm scale bar

The diameters and lengths of the $Zn_{1-x}Mg_xO$ NWs varied from: 20-95nm and 0.5-1.0µm; 40-80nm and 0.6-1.0µm; 45-150nm and 0.5-1.0µm; 40-90nm and 0.5-0.9µm, corresponding to x = 0.04, 0.09, 0.19 and 0.29, respectively. No secondary growth seeded from the nanowires (secondary nucleation) was observed.

Mg contents in the different samples of Fig. 3.1 (b) – (e) are summarized in Table 3.2. Mg mole fractions were measured using energy dispersive spectroscopy (EDS) in a Scanning Electron Microscope (SEM). Table 3.1 & Table 3.2 intuitively evidence that Mg mole fraction can be increased as high as x=0.19 by simply increasing Cp_2Mg/DEZn ratio, i.e. by introducing more Mg source to the chamber compared to Zn source while keeping all the other growth parameters constant. In order to achieve 29% Mg mole fraction, a thin layer with a CP_2Mg/DEZn ratio of 200 was deposited on top of the $Zn_{0.71}Mg_{0.19}O$ NWs followed by a Mg drive-in at 900°C. The MgO-ZnO phase diagram suggests that raising the growth/Mg activation temperature should result in higher Mg incorporation. However, in this work Mg mole fraction was limited to 29% and this limitation is attributed to (i) the constraint imposed by the mass flow controllers in the MOCVD that restricted Mg flow rate (max. of 200 sccm) and (ii) growth/ Mg activation at temperatures beyond 1000˚C

could significantly change the morphology and the phase of the otherwise wurzite – ZnO films. On ZnO NWs grown on GaN/Sapphire and characterized under high temperature XRD, ranging from 25° C to 1200° C. the corresponding peak to wurtzite ZnO 002 was shifted toward larger 2θ angle until the temperature reached 1200° C where no wurtzite ZnO 002 diffraction peak could be identified suggesting a change in phase.

Table 3.2: - EDS taken on SEM for Mg mole fraction of 5, 9, 19 and 29%.

Sample #	Wt %		a.m.u.		Mole		Mg mole fraction
	Mg	Zn	Mg	Zn	Mg	Zn	
b	0.61	31.89	24.3	65.4	0.0251	0.4876	4.90%
c	1.55	41.89	24.3	65.4	0.0638	0.6405	9.10%
d	1.23	14.04	24.3	65.4	0.0506	0.2147	19.10%
e	0.07	0.46	24.3	65.4	0.0029	0.007	29.06%

The NWs in sample (e), that exhibited this high Mg content, were further scrutinized by means of EDS in a Transmission Electron Microscope (TEM). The results were strikingly similar as shown in Fig 3.2-a, although, the high resolution TEM revealed some more details. The picture shown in Fig 3.2-b obtained from TEM measurements suggests that the Mg mole fraction gradually increasing along the nanowire, being 0.16 at the bottom and 0.29 at the top of the nanowires which is understood as follows As outlined in the experimental section, Mg concentration of 0.29 was achieved by first depositing a layer of MgO on top of the ZnMgO NWs, followed by diffusion/drive-in and anneal at 900˚C. Prior to the drive-in step, the MgO layer is expected to accumulate predominantly on top of the NWs since the high density of NW arrays prevent MgO from reaching to the bottom

of the NW array, i.e. “shadow effect” The non-uniformity of Mg content along the NW axes prevails during the drive-in/ annealing steps and could be due to the gradient in temperature perpendicular to the substrate or along the growth axis during these steps. Variation in temperature can give rise to a diffusion or mass transfer of defects, moving toward high temperature for vacancies or toward low temperature for interstitial atoms [6]. It is important to note that this assumption is only valid for vacancies with formation energy larger than the activation energy of their migration. Larger diffusion coefficients for Mg at higher temperatures have been reported by Yang et al. the diffusion coefficient being 0.052x10-14 cm2/s at 750˚C and 3.026x10-14 cm2/s at 950˚C [7]. Their observation is also consistent with Ohtomo *et al.* who studied Mg diffusion in ZnMgO films annealed at a temperature range of 700˚C and 850˚C as the segregation of MgO started beyond that point [8].

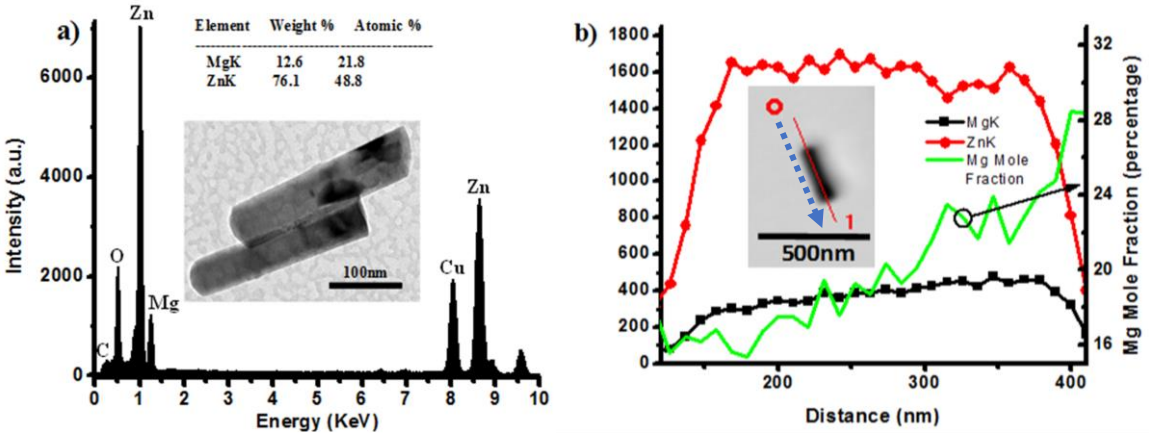

Fig. 3.2:a EDS of ZnMgO with 30% Mg mole fraction taken under TEM. 2-b) Shows the EDS as a function of distance taken along the ZnMgO NW. The Mg and Zn concentrations, (intensity, arbitrary units) (left y-axis) and the Mg mole fraction (right y-axis) are plotted as a function of distance along the NW. The Mg mole fraction increases moving from the bottom to the top of the nanowire as indicated by the blue arrow in the inset. The TEM sample was prepared by mechanical exfoliation, removing the CS structures from the p-Si substrate and depositing them on TEM copper grids. There is a likelihood that part of the nanowire was cut off in that process.

Figure 3.3-a shows room temperature PL of $Zn_{1-x}Mg_xO$ NWs with varying Mg mole fractions where the peaks resolved using Lorentzian fits. The PL emission peaks (Epeak) at 380nm, 360nm, 328nm, and 297nm correspond to the mole fraction (MF) = 0.04, 0.09, 0.19, and 0.29, respectively. The measured FWHM were 2.05nm for MF = 0.04, 2.43nm for MF = 0.09, 2.25nm for MF = 0.19, and 3.63nm for MF = 0.29 that show generally an increasing trend with increasing Mg mole fraction. Similar observations were also made by Reddy et al. [9] and Wassner et al. [10] which simply means that it is increasingly more challenging to maintain PL quality as Mg mole fractions introduced go up. The substitution of Zn atom by Mg atom behaves as an isoelectric impurity randomly incorporated into the crystal, disrupting the lattice periodicities due to different ionic radii and electronegativities. Consequently, it leads to localization of energy and results in broadening of the Epeak. But not only the FWHM increases with Mg mole fraction, the NBE due to free exciton emission shifts to shorter wavelengths along with a decrease in the intensity of PL transitions. Figure 3.5-a and 3.5-b summarize the bandgap energy and FWHM of the PL spectra as a function of the Mg mole fraction mentioned above.

The PL Epeak at 389nm is associated with near bandgap UV emission from the underlying ZnO epilayer. For the case of x = 0.29, some other peaks are observed, namely at 290, 300 and 330 nm that may be attributed to the non-uniform distribution of Mg along the length of the NWs. The peak at 310nm is an artifact of the measurement set up as the bandpass filter used in conjunction with the HgXe lamp in this study had weaker attenuation in that frequency band. Growth parameters other than only Cp_2Mg/DEZn ratio will be tweaked in our future work to see if better PL quality can be attained for higher Mg content samples as well.

The PL spectra at longer wavelengths are shown in Fig 5.3-b, that were measured using a HeCd laser as light source. The peak located at 538 nm resulted in green emission due to transition of electrons from the shallow donor level (oxygen vacancies) to shallow acceptor level (Zn vacancies) [11-12]. Transitions between zinc vacancies ($V_{Zn}^{2-} \rightarrow V_{Zn}^{-}$) at 2.1 eV gives rise to the peak observed at 587 nm (yellow emission) [13]. It is to be noted that the peaks at 538 nm and 587 nm were present in all samples and are associated with the underlying ZnO epilayer. The degradation of optical quality with increasing Mg concentration is consistent with the observed broadening of FWHM of XRD spectra and is discussed next.

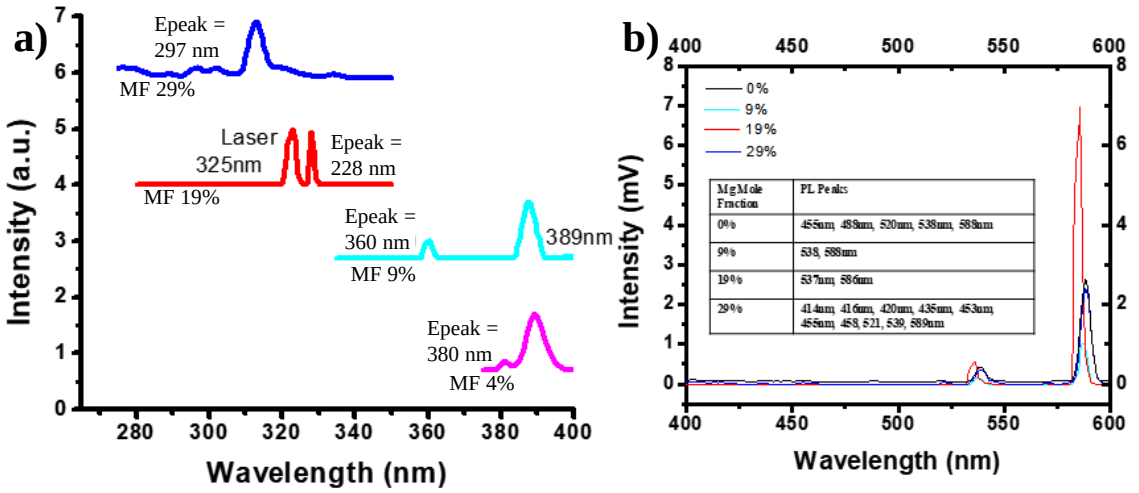

Fig. 3.3:a Room Temperature PL measurement of Zn1-xMgxO NWs. The ZnMgO NWs shown emission peaks (Epeak) at 380nm, 360nm, 328nm and 297nm, corresponding to the Mg mole fraction (MF), MF = 0.04, 0.09, 0.19 and 0.29, respectively. The peak at 325nm for x = 0.19 corresponds to the light source and 389 for x = 0.04 correspond to the NBE of ZnO thin film. 3-b shows the PL for longer wavelength taken using the HeCd laser.

X-ray diffraction for wurtzite $Zn_{1-x}Mg_xO$ NWs grown on Si (100) is shown in Fig. 3.4. Diffraction peaks associated with ZnO oriented along (100, 101, 102, 110, 103) are observed. Comparing the intensities, it could be inferred that most of the NWs are oriented along the vertical axis; with 94.56% (x = 0.04), 91.8% (x = 0.29), 73% (x = 0.09), and

45.5% (x = 0.19); perpendicular to the substrate. As the lattice mismatch increases with larger Mg mole fraction, the structure relaxes through defects/dislocations, propitiating the growth of vertically aligned nanowires. No diffraction peak associated with the cubic crystal phase of MgO, specifically at ~42° (2θ) and ~61° (2θ) (corresponding to the planes (002) and (220), respectively), were observed in contrast to the growths reported by most authors such as, H. Tang et al. [14] and H.C. Hsu et al [15], suggesting that MgO fully diffused into ZnO NWs during the drive-in step at 900˚C.

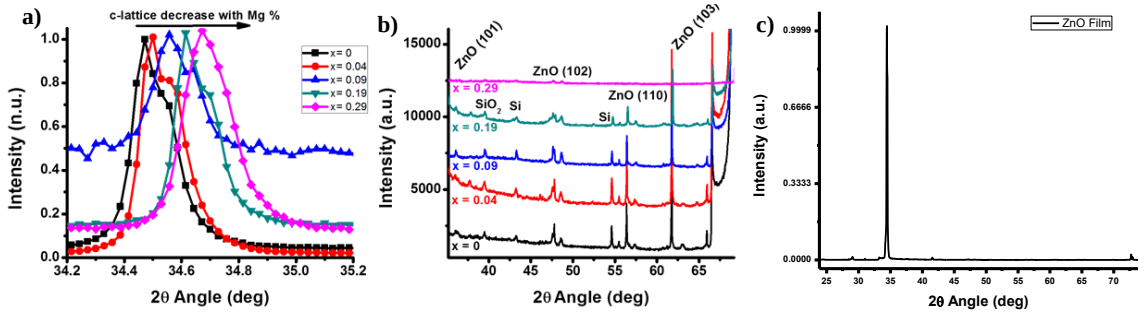

Fig. 3.4:a XRD of $Zn_{1-x}Mg_xO$ NWs with different Mg mole fraction, 0 % (black), 4 % (red), 9% (blue), 19% (navy) and 29% (magenta) with an intensity of 5,980(a.u.) of ZnO oriented along (002). 3.4-b shows diffraction peaks associated with ZnO (101, 102, 110 and 103). 3.4-c shows the XRD for the ZnO film with a peak located at 34.4377° (2θ) which correspond to a c-lattice constant of 5.204Å

The c-lattice constant and the resulting in-plane bi-axial stress on ZnMgO NWs were calculated from Braggs' law and Hooke's law, respectively, and are shown in Fig 5(c-d). The c-lattice constant decreases with increasing Mg mole fraction with a concomitant increase in stress. The c-axis lattice constant (as obtained from our experimental data), is shown in Fig. 5(c), and can be expressed as:

$$c_{Zn_{1-x}Mg_xO} = 5.1989 - 0.11x + 0.045x2 \text{ Å} \quad (3.1)$$

suggesting the c-axis lattice constant of the wurtzite phase MgO to be 5.1338 Å in agreement with the theoretically predicted value of 5.1 Å [16] . The c-lattice constants were calculated with +/- 0.005Å of uncertainty taking into account the error from energy

resolution, experimental misalignment, detector resolution, and peak width and intensity [17].

The error derived from the energy of the primary beam and the experimental misalignment contributes the least to the uncertainty in the lattice parameter calculations, with about $5x10^{-5}$ and $3.4\ x10^{-4}$ (degrees), respectively. The largest variation in the angle of diffraction comes from the resolution of the detector (~0.029 degrees) and from the peak width/intensity. According to Kujofsa et al., calculations for uncertainty can be made by taking into account the effective number of counts (N_{eff}) and the full-width-at-half-maxima (FWHM) [18]. The uncertainty in the measured peak position is proportional to the peak width, $\Delta\theta = C_P\beta$, where β is the FWHM (from the Gaussian fit) and C_p is a constant of proportionality given by,

$$C_P = \frac{1}{2\sqrt{ln(2)}}\sqrt{-ln\left(1-\frac{1}{\sqrt{N_{Eff}}}\right)} \tag{3.2}$$

with N_{eff} equal to the number of counts. Table 3.3 summarizes the uncertainty in the *c* and *a*-lattice calculations as a function of Mg mole fraction.

Table 3.3: - Summary of the c and a-lattice constant uncertainty taking into account taking into account the error from energy resolution, experimental misalignment, detector resolution and peak width and intensity.

Mg mole fraction	c-lattice constant	a-lattice constant
x = 0.04	5.1952 ± 0.0047	3.2538 ± 0.0089
x = 0.09	5.1875 ± 0.0058	3.2517 ± 0.0092
x = 0.19	5.1793 ± 0.0052	3.2568 ± 0.0102
x = 0.29	5.1707 ± 0.0055	3.2602 ± 0.0110

The a-lattice constant, shown in Fig 3.5(c & e), of the NWs, are estimated from the calculated c-axis lattice constant and the Miller indices for the ZnO (102) crystal plane

obtained from XRD measurements. The peak for ZnO (110) was not used to calculate a-lattice constant in order to maintain consistency, as the sample x = 0.04 and 0.29, do not have a diffraction peak at (110). The a-lattice constants have an uncertainty of +/- 0.009 and 0.01Å for Mg mole fraction of x = 0.04 – 0.09 and 0.19 – 0.29, respectively, with the larger uncertainty coming from the low intensity of the diffraction peak at 47° (2θ) and from the resolution of the scan 0.02˚ (for speed of data collection). For low Mg mole fraction (x < 0.04) the a-axis lattice constant follows a linear combination of ZnO-MgO lattice constants while keeping a constant lattice volume. With Mg mole fraction exceeding 0.04, the cell volume decreases slightly due to the substitution of Mg with a slightly smaller ionic radius (Mg^{++} - 0.65A) [19] onto Zn sites with a slightly larger ionic radius (Zn^{++} - 0.74A) [19]. This change in lattice constant has been observed by other researchers but was not necessarily explained, although the a-lattice constant may be within the estimated error percentage. For example, Ohtomo [20] et al. and Wassner [21] et al. reported a-lattice constants of ZnMgO films increasing with Mg mole fraction and slightly decreasing after x = 0.09. The change in lattice constants as a result of differences in the ionic radius is also observed in other material platforms, such as highly doped (boron) silicon [22].

Further increment in Mg concentration results in a continuous increase of the a-axis lattice constant keeping the cell volume more or less unchanged. Opposite observations that showed an increase in the a-axis lattice constant along with an increase in the cell volume, was made by Fukumura et al., when Mn^{++}, with a larger ionic radius, was incorporated in ZnMnO [23]. It is to be noted that assuming a constant lattice volume and the c-axis lattice constant in biaxial stress formulation, over-estimates the a-axis lattice constant (Fig. 3.5-e). The stiffness coefficients are extracted from the lattice constants and

the strain. The extracted elastic constants from the experimental data differ from the theoretical stiffness coefficients reported in the literature, as can be observed from Table 3.4. The theoretical stiffness coefficients are determined assuming a constant lattice volume (CLV) as shown in Figure 3.5-e. In order to match the a-axis lattice constant extracted from XRD measurements to that obtained using strain formulation necessitated calculation of the modified elastic constants (MEC) as presented in Table 3.4. MECs take into account the change in the cell volume, specifically the variation of the a-lattice constant with Mg mole fraction.

The a-axis lattice constant, for Mg concentration in the range of x = 0 to x = 0.09 and x = 0.09 to x = 0.29, are expressed in eq. 3.3 & 3.4, respectively as:

$$a_{Zn_{1-x}Mg_xO} = 3.25 + 0.15589x - 1.52x2 \text{ Å} \quad (3.3)$$

$$a_{Zn_{1-x}Mg_xO} = 3.2482 + 0.0425x \text{ Å} \quad (3.4)$$

This suggests the a-axis lattice constant of the wurtzite phase MgO to be 3.2907 Å in agreement with the theoretically predicted value of 3.30 Å [24].

Table 3.4: $Zn_{1-x}Mg_xO$ Stiffness Coefficient. *Ref 25, **Fit to Experimental Data

x	C11* [Pa]	C12* [Pa]	C13* [Pa]	C13** [Pa]	C33* [Pa]	C33** [Pa]
0	2.38E+11	1.06E+11	8.40E+10	3.86E+11	1.21E+11	1.50E+11
0.04	2.37E+11	1.05E+11	8.42E+10	1.08E+11	1.25E+11	1.54E+11
0.09	2.35E+11	1.04E+11	2.44E+10	1.30E+11	1.30E+11	4.75E+11
0.19	2.32E+11	1.01E+11	2.48E+10	7.08E+10	1.40E+11	6.38E+11
0.29	2.28E+11	9.85E+10	2.52E+10	5.80E+10	1.50E+11	5.80E+11

Measured Hall mobility (μ), shown in Fig 3.5(f), decreases monotonically with increasing Mg-mole fraction, from 32 cm^2/V-s for ZnO to 3 cm^2/V-s for $Zn_{0.71}Mg_{.29}O$. The measured mobility of 32 cm^2/V-s for ZnO nanowires is higher compared to the

reported values of 13.28 [26] cm^2/V-s and 28.68 cm^2/V-s [27]. The rather high mobility could be attributed to high-quality nanostructures with reduced stress as evident from the narrow FWHM of the measured XRD and related PL measurements. An FWHM of ~2nm in the PL peak for ZnO NBE indicates excellent crystal quality with insignificant secondary growth as compared to 10nm [28] and 11nm [29]. As reported by Metz et al., narrow FWHM is correlated to higher mobility [30]. The quality of the ZnMgO nanostructures is also evident from the PL measurements, where the FWHM is 14.7 nm at NBE. The ratio of the intensity between the NBE (I_{NBE}) and native defects (I_{ND}) observed at 538nm (oxygen vacancy), I_{NBE}/I_{ND} ~ +150, suggests low native defects, contributing to the observed higher mobility.

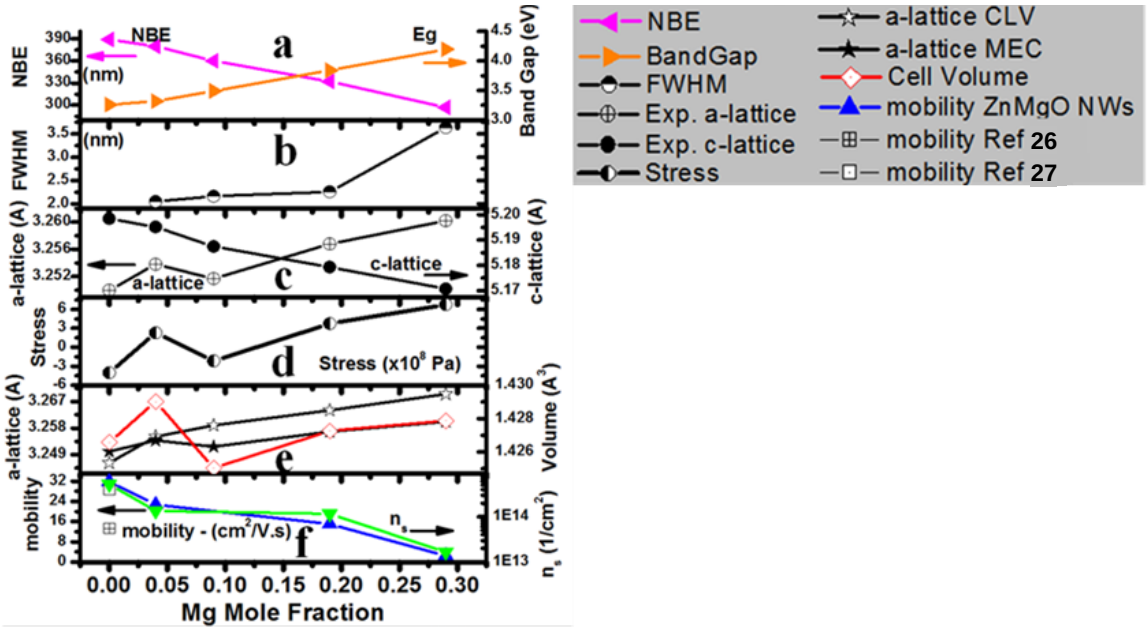

Fig. 3.5: Shows a summary of the crystal and optical properties as a function of Mg concentration. (a) Shows the wavelength of near band emission decreasing as Mg incorporation increases, the band gap (in eV) is shown on the right axis. (b) The FWHM of the PL increasing with increment in Mg mole fraction. (c) The experimental a and c-lattice constant are plots as a function of Mg concentration. (d) Shows the corresponding bi-axial stress. (e) The a-lattice parameter with modified elastic constant (MEC) is compare on the left axis to the calculated a-lattice with constant lattice volume (CLV) from bi-axial strain using the experimental c-lattice constant from ZnO (002). While on the right side, the cell volume is plotted as a function with Mg mole fraction. (f) Shows the decrease of electron mobility and sheet carrier concentration as a function of Mg mole fraction. *The white squares correspond to the mobility of ZnO reported on Ref. 26-27.*

With increasing Mg mole-fraction, mobility degrades as observed in Figure 3.5(f) and may be explained as follows. With increasing Mg mole fraction, which is verified using EDS, NBE increases along with an increase in the a-axis lattice constant, giving rise to an increase in the effective mass with a concomitant decrease in mobility. Nevertheless, increasing effective mass may not be the primary reason for mobility degradation with increasing Mg mole fraction. Assuming a Hall scattering factor (r_H) of one [31] makes the low field mobility to equal Hall mobility, allowing the determination of momentum relaxation time using the standard formulation as shown in eq. 5 [32].

$$\mu = \frac{q}{m^*}\,\tau \tag{3.5}$$

Where μ is the carrier mobility, q is the elementary charge, m^* is the effective mass and τ is the momentum relaxation time, that decreases from 58.3nsec to 5.75 nsec for Mg mole fraction increasing from 0 to 0.29. More frequent momentum relaxation scattering along with a concomitant decrease of sheet carrier concentration due to surface traps or other associated scattering sites may explain the decrease in observed mobility with increasing Mg mole fraction. K. Matsubara [33] et al. and K. Maeijima [34] et al. attributed the observed lower mobility to increase in resistivity due to decreasing carrier concentration.

3.4 Conclusions

$Zn_{1-x}Mg_xO$ NWs was grown on p-Si in the absence of any metal catalyst using MOCVD with Mg mole fraction varying from 0.04 to 0.29. The physical structure of the NWs remained significantly uniform for the range of Mg mole fraction investigated, with diameter and length distribution in the range of (40-180nm) and (0.5-1.5μm). The c-lattice constant decreased for larger Mg concentration. The absence of MgO phase confirms the substitution of Zn^{2+} ions by Mg^{2+}, without modifying Zn tetrahedral bonding. It also confirms a complete diffusion of Mg into ZnMgO for x = 0.29. PL spectra of the NWs show strong and narrow excitonic emission peaks varying from 297nm to 360nm corresponding to the Mg incorporation varying from x = 0.09 to x = 0.29. The small FWHM of 3.63nm of the PL data for Mg mole fraction of 29% confirmed the outstanding crystal quality of the ZnMgO NWs. Also, the extremely weak deep level emission observed for longer wavelengths indicates the high optical quality of the grown ZnMgO NWs. Hall measurement shows a decrease in electron mobility with increasing Mg concentration.

Based on the results obtained from the present study, the following conclusions can be made:

- The c-lattice constant decreased for larger Mg concentration while the a-lattice constant increased with larger Mg mole fraction.
- If the lattice volume is assumed to remain constant as the Mg mole fraction increases, estimation from the stiffness coefficient would results in under estimation of the lattice parameters.

- A more accurate stiffness coefficients taking into account the variation in the lattice volume are presented as a function of Mg mole fraction, from experimental data.

References:

1. K. Ogata, K. Maejima, S. Fujita, et al., J. Electron Mater. 30, 659 (2001)
2. C.K. Lau, S.K. Tiku, and K.M. Lakin, J. Electrochem. Soc. 127, 1843 (1980)
3. R. Piotrkowski, E. Litwin-Staszewska, T. Suski, and I. Grzegory, Physica B 308-310, 47 (2001)
4. S.-H. Jeong, B.S. Kim, and B.-T. Lee, Appl. Phys. Lett. 82, 2625 (2003)
5. S.F. Yu, C. Yuen. S.P. Lau, and H.W. Lee, Appl. Phys. Lett. 84, 3244 (2004)
6. J.A. Brinkman, Phys. Rev. 93, 345 (1954)
7. L.L. Yang, Q.X. Zhao, G.Z. Xing, D.D. Wang, T. Wu, M. Willander, I. Ivanov and J.H. Yang, Appl. Surf. Sci. 257, 8629 (2011)
8. A. Ohtomo, R. Shiroki, I. Ohkubo, H. Koinuma, and M. Kawasaki, Appl. Phys. Lett., 75, 4088 (1999)
9. A.S. Reddy, P. Prathap, Y.P.V Subbaiah, K.T. Ramakrishna, and J. Yi, Thin Solid Films 516, 7084 (2008)
10. T.A. Wassner, B. Laumer, S. Maier, A. Laufer, B.K. Meyer, M. Stutzmann, and M. Eickhoff, J. Appl. Phys. 105, 023505 (2009)
11. P.S. Venkatesh, V. Purushothaman, S.E. Muthu, S. Arumugam, V. Ramakrishnan, K. Jeganathan, and K. Ramamurthi, Cryst.Eng.Comm, 14, 4713 (2012)
12. M. Willander, O. Nur, N. Bano, and K. Sultana, New J. Phys. 11, 125020 (2009)

13. Y. Kamada, M. Furuta, T.K. Hiramatsu, T. Kawaharamura, D. Wang, S.I. Shiwakawa, C. Li, S. Fujita, and T. Hirao, Appl. Surf. Sci. 258, 695 (2011)
14. H. Tang, Z. Ye, and H. He, Mater. Lett. 62, 1393 (2008)
15. H.-C. Hsu, C.-Y. Wu, H.-W. Cheng, and W.-F. Hsieh, Solid State Commun. 131, 371 (2004)
16. Q. Xu, X.-W. Zheng, W.-J. Fan, S.-S. Li and J.-B. Xia, Comp. Mater. Sci. 44, 72 (2008)
17. D. Kriegner, E. Weinstersberger, K. Kawaguchi, J. Walletin, M.T. Borgstrom and J. Stangl, Nanotechnology 22, 425704 (2011)
18. T. Kujofsa, and J.E. Ayers, Int. J. Hi. Spe. Ele. Syst., 24, 1550007 (2015)
19. B.-C. Oh, W.-C. Choi, S. Park, Y.-o. Kim, and T.-K. Oh, Appl. Microbiol. Biot. 63, 362 (2004)
20. A. Ohtomo, M. Kawasaki, T. Koida, K. Masubuchi, Y. Sakurai, Y. Yoshida and Y. Segawa, Appl. Phys. Lett. 72, 2466 (1998)
21. T.A. Wassner, B. Laumer, S. Maier, A. Laufer, B.K. Meyer, M. Stutzmann and M. Eickhoff, J. Appl. Phys. 105, 023505 (2009)
22. M. Grundmann, The Physics of Semiconductors, An Introduction Including Nanophysics and Applications, (Springer-Verlag Berlin Heidelber 2010) Vol. 2
23. T. Fukumura, Z. Jin, A. Ohtomo, H. Koinuma, and M. Kawasaki, Appl. Phys. Lett 75, 3366 (1999)
24. Q. Xu, X.-W. Zheng, W.-J. Fan, S.-S. Li and J.-B. Xia, Comp. Mater. Sci. 44, 72 (2008)
25. S.-H. Juang, and S.F. Chichibu, J. Appl. Phys. 112, 073503 (2012)
26. Z.Y. Zhang, C.H. Jin, X.L. Liang, Q. Chen, and L.-M. Peng, Appl. Phys. Lett. 88, 073102 (2006)

27. J. Goldberger, D.J. Sirbuly, M. Law, and P. Yang, J. Phys. Chem. B 109, 9 (2005)
28. W. Lee, M.-C. Jeong and J.-M. Myoung, Acta Mater. 52, 3949 (2004)
29. D.-I. Suh, C.C. Byeon, and C.-L. Lee, Appl. Surf. Sci. 257, 1454 (2010)
30. A.W. Metz, J.R. Ireland, J.-G. Zheng, R.P.S.M. Lobo, Y. Yang, J. Ni, C.L. Stern, et al., J. Am. Chem. Soc. 126, 8477 (2004)
31. H. Morkoc, and U. Ozgur, Zinc Oxide: Fundamentals, Materials and Devices Technology, (Wiley-VCH, Germany, 2009)
32. W. Zhu, V. Perebeinos, M. Freitag, and P. Avouris, Phys. Rev. B 80, 235402 (2009)
33. K. Matsubara, H. Tampo, H. Shibata, A. Yamada, P. Fons. K. Iwata, and S. Niki, Appl. Phys. Lett 85, 1374 (2004)
34. K. Maejima, H. Shibata, H. Tampo, K. Matsubara, and S. Niki, Thin Solid Films 518, 2949 (2010)

Chapter 4

Co-axial Core-Shell ZnMgO/ZnO Nanowires

This chapter presents the growth of co-axial $Zn_{1-x}Mg_xO$/ZnO core–shell structures, on p-Si substrates using MOCVD. The crystal structure of the core-shell nanowires is analyzed using SEM, TEM and XRD. In addition, the core-shell structures are used as a gas sensor, specifically for methanol and acetone, and compared to ZnO NRs based device. The underline point defect associated to an enhancement in the sensing mechanism is identified and confirmed with PL data.

4.1 Growth $Zn_{1-x}Mg_xO$/ZnO Co-axial Core-Shell Structures

ZnMgO/ZnO core/shell (CS) structures are grown on p-Si substrates using MOCVD synthesis. A ZnO thin film used as a seed layer was grown as described in section 2.1, at 300°C. The temperature was raised to 650° C and the pressure was decreased to 4 Torrs for the growth of the ZnMgO core structure seeded on the thin film using a ratio of 1:10 of DEZn:Cp_2Mg, Cp2Mg (Bis(cyclopentadienyl)magnesium) being the Mg source. The Zn/Mg ratio can be varied to tune the Mg mole fraction of the core as shown in table 4.1. A 10 min drive-in of MgO using 200 sccm of Cp_2Mg and 500 sccm of N_2O was performed to increase the Mg mole fraction. The growth was followed by Mg activation at 800° C for 10 min in nitrogen ambient. Finally, the ZnO shell was grown at 300° C using similar parameters used during the growth of the seed layer.

Table 4.1: Variation of precursor rates used to achieve Mg mole fraction of 2, 5 and 10%

Mg mole fraction	DEZn Flow Rate	Cp_2Mg Flow Rate
x = 0.02	10 sccm	150 sccm
x = 0.05	12 sccm	175 sccm
x = 0.10	10 sccm	200 sccm

4.2 Characterization

Figure 4.1-A shows the scanning electron microscopy (SEM) images of the ZnMgO/ZnO CS structure grown using MOCVD. The ZnMgO/ZnO CS structures are mostly vertically aligned with respect to the basal plane and have sharp tips (ZnO terminated). Figure 4.1-B shows the coaxial shape of the CS structure. Energy-dispersive X-ray spectroscopy (EDS) with excitation energy of 10 keV confirms the CS structure by showing 8–10% Mg in the core (inset of figure 4.1-B) and 0% Mg in the shell. The Mg concentration of the core can be tuned by adjusting the Mg/Zn ratio during growth and by varying the annealing time. High resolution EDS was also carried out under transmission electron microscope (TEM) confirming 8–10% Mg incorporation at the core and 0% Mg incorporation at the shell, as illustrated in figure 4.1-C. To assess the co-axial CS interface, bright field images are taken using TEM as shown in figure 4.1-D. The TEM sample was prepared by mechanical exfoliation, removing the CS structures from the p-Si substrate and depositing them on TEM copper grids. The diameter of the core (ZnMgO) and the thickness of the shell (ZnO) structures are around 80–100 nm and 20–40 nm, respectively. The total length of the structure is estimated to be in the range of 0.8–1.2 μm. The abrupt interface between the CS is highlighted by arrows. The contrast between the ZnMgO core and ZnO shell is not

as pronounced as is observed for typical heterostructures, owing to a similar crystal composition possibly due to similar lattice constants. The inset of figure 4.1-C shows the selected area electron diffraction (SAED) measurement indicating the structure is single crystalline. These results suggest that ZnO was epitaxially grown on $Zn_{0.90}Mg_{0.10}O$ NWs resulting in a low or non-defect nano-structure.

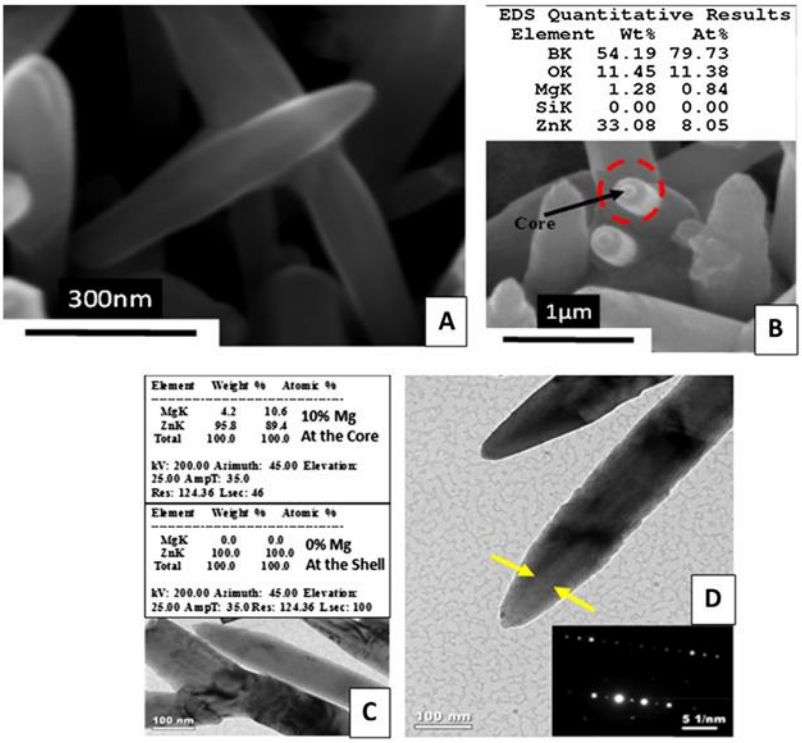

Fig. 4.1: (A) SEM of co-axial ZnMgO/ZnO core–shell structure showing a clean surface and sharp tips grown using MOCVD. (B) SEM shows the core–shell structure. The diameter was measured to be 80–100 nm for the ZnMgO core and 20–40 nm for the ZnO shell. The inset shows EDS of the core and shell, reflecting 10% Mg at the core, 0% at the shell. (C) EDS of ZnMgO/ZnO core–shell structure with nm scale resolution carried out under TEM confirming the Mg mole fraction at the core of the CS. (D) Bright field TEM image shows the co-axial core–shell structure; the inset shows SAED pattern suggesting single crystalline structure.

Furthermore, the Mg mole fraction was measured along the radial axis as shown in figure 4.2. The counts of Zn and Mg are plotted in the lefty-axis as function of distance,

while the Mg mole fraction is plotted in the right-y-axis. As expected, the Mg mole fraction remains almost constant at the center, while diminish as approach the edges. This suggests a core of 72nm and a shell of 44nm.

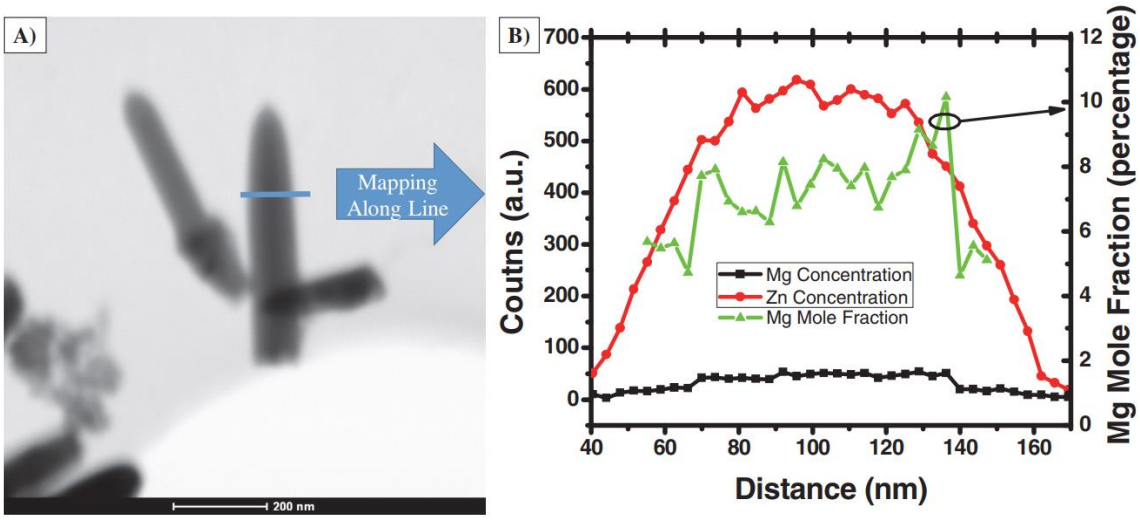

Fig. 4.2: EDS shows the Zn (red circles) and Mg (black square) concentration on the left y-axis, as function of distance. The Mg mole fraction (green triangle) are shown on the right y-axis, with a Mg mole fraction at the core in the range of 6 – 8 % and diminishing as it moves to the edges.

To further investigate the crystal structure of the ZnMgO/ZnO CS nanowires, X-ray diffraction measurement was performed using a Bruker D-8 Advanced X-ray diffractometer with a wavelength $\lambda = 1.5406$ Å corresponding to the Cu Kα. Figure 4.3-A shows the XRD pattern for the ZnMgO/ZnO CS structure grown on p-Si substrates using MOCVD with $Zn_{0.98}Mg_{0.02}O$ at the core. No peak corresponding to cubic MgO crystal or other alloys, such as $Zn_{1.7}SiO_4$(Zn,Mg)$_{1.7}SiO_4$ [1] are observed, suggesting the absence of those impurities in the grown materials. Low intensity peaks are observed, corresponding to ZnO (101), (102), (110), (103) and (200). Similar diffraction patterns were observed for 5 and 10 % Mg at the core. Figure 4.3, B-D shows the dominant peak related to ZnO (002) at 34˚ (2θ), supporting the vertical alignment of the NWs observed in the SEM images. The

peaks corresponding to ZnO and ZnMgO are observed to overlap since their lattice constants are very similar. A peak resulting from a combination of multiple peaks due to diverse crystal planes and/or materials may be decomposed using a Lorentzian fit to identify the constituent peaks, thereby providing the maximum (where the c-lattice constant is calculated) and the full-width at half-maximum (FWHM) for each of the peaks. The high resolution XRD at 34˚ shows a split in the diffraction peak confirming the ZnMgO/ZnO CS structure in agreement with the SEM, EDS and TEM analysis, varying depending upon Mg mole fraction. The peak attributed to the core-ZnMgO, shifted from 34.4635˚ to 34.5580˚ for Mg mole fraction of 2% and 10% from which the c-lattices constants were estimated to be 5.2005 and 5.1867Å. The peak related to the shell (ZnO) varied from 34.3784 for 2% Mg to 34.4710 for 10% Mg, suggesting a c-lattice constant of 5.21 to 5.1995Å, respectively. The relative variation of $Zn_{1-x}Mg_xO$ c-lattice constant is in accordance to Ohtomo et al. [2] The c-lattice constant of the core is consistent with ZnMgO NWs grown on p-Si (5.1889Å, 10%Mg), [3] (5.191Å, 12% Mg) [4] and on c-sapphire (5.1873Å, 8% Mg). [5] The FWHMs were estimated to be 0.0641˚ (θ), 0.0685˚ (θ) and 0.0818˚ (θ), corresponding to 2%, 5% and 10% Mg at the core, respectively.

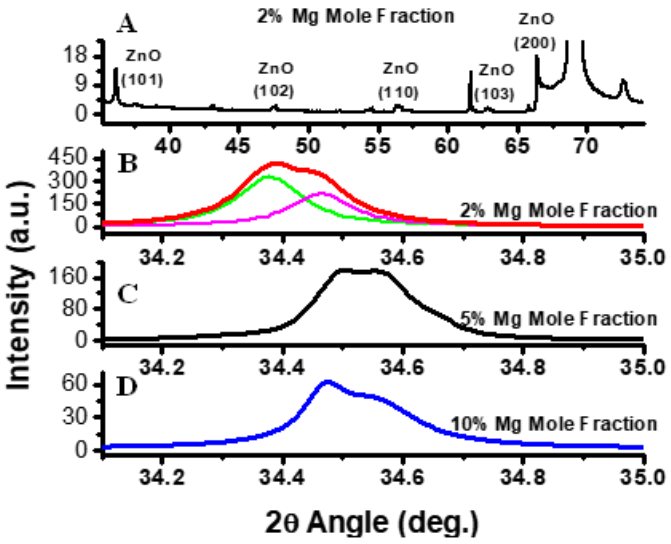

Fig. 4.3: XRD of $Zn_{0.98}Mg_{0.02}O$/ZnO CS structure with diffraction pattern associated to ZnO (101, 102, 110, 103, 200) in the absence any MgO crystal phase. Fig B – D) Shows the diffraction peak corresponding to ZnO oriented along (002) shifted to higher angle (decreasing c-lattice constant) with larger Mg mole concentration at the core.

4.3 Gas Sensing

4.3.1 Device-Fabrication and Operation

Figure 4.4 shows the schematic of the fabricated $Zn_{1-x}Mg_xO$/ZnO CS gas sensor operated at room temperature. For each device, three different Mg mole fractions were used in the core of the CS structures, 0.02, 0.05 and 0.1, which will be referred as CS-0.02, CS-0.05 and CS-0.1, respectively, in the rest of the discussion. The ZnMgO/ZnO CS detectors were fabricated by depositing indium on p-Si, serving as the bottom metal contact, and mounting the sample on a chip holder. Indium dots were deposited on the ZnMgO/ZnO surface using a home-built indium-soldering station, serving as the top metal contact. A load resistance was connected in series with the gas sensor (1 kΩ) to form a voltage divider. The gas sensor was biased with 2V while the output voltage was measured across the load resistor.

Variation on the resistance of the sensor upon varying concentration of gas molecules is observed at the output voltage of the load resistor. When the device is exposed to air, the O_2 molecules (in the air) get adsorb or trap in the oxygen vacancies states. With gas reaching the sensor surface, methoxy species and formaldehyde molecules are formed by dissociative chemisorption of methanol. [6] Subsequently, the mentioned species gives rise to formic acid liberating an electron. This electron enters into the conduction band and lowers the resistivity of the sensor material. [7] The oxygen vacancies can enhance the oxygen molecular absorption and promote the dissociative adsorption, in which one of the oxygen atoms fills the original oxygen vacancies. [8]

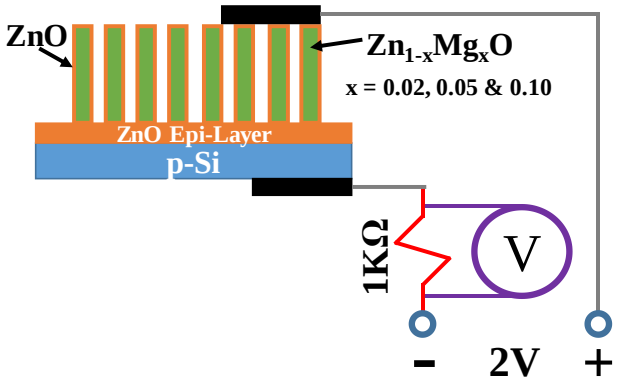

Fig. 4.4: Shows the schematic of the fabricated Zn1-xMgxO/ZnO CS gas sensor operated at room temperature. The ZnMgO/ZnO CS detectors were fabricated by depositing indium used as bottom and top contacts. The response of the device was measured through a load resistance of 1 kΩ

4.3.2 Device-Performance

Figure 4.5 shows the voltage variation of the gas sensor with/without methanol gas. The response time for adsorption and desorption of gas molecules is shown on figure 4 for each of the Mg concentration at the core. During desorption of the methanol molecules, two

transitions are observed for the CS-0.02 and CS-0.05 based sensor while a single transition for the CS-0.1 based sensor. The activation energy of the defects are calculated from these transition times using the following equation [9]:

$$t_d = \frac{1}{\sigma_n \, v_{th} \, N_C \, e^{-(E_c - E_T)/kT}} \tag{4.1}$$

where t_d (= 0.37 and 0.48s for CS-0.02, 5.98 and 0.89s for CS-0.05 and 0.130s for CS-0.1) is the detrapping time, σ_n (= 1.6x10^{-13} cm^{-2} [10]) is the electron capture cross section, v_{th} = thermal velocity ($\sqrt{3kT/m_e^*}$), N_C (= 1x10^{18} cm^{-3}) is the effective density of states, E_c and E_T are the conduction and trap energy levels, and m_e^* (= 0.321 for CS-0.02, 0.3216 for CS-0.05 and 0.3240 for CS-0.1) is the electron effective mass. The activation energy for CS- 0.02, CS-0.05 and CS-0.1 - gas sensor is approximately 1.19-1.20eV, 1.22-1.26eV and 1.16eV, respectively. This activation energy corresponds to doubly charged oxygen vacancy (Vo^{2+}). [11]

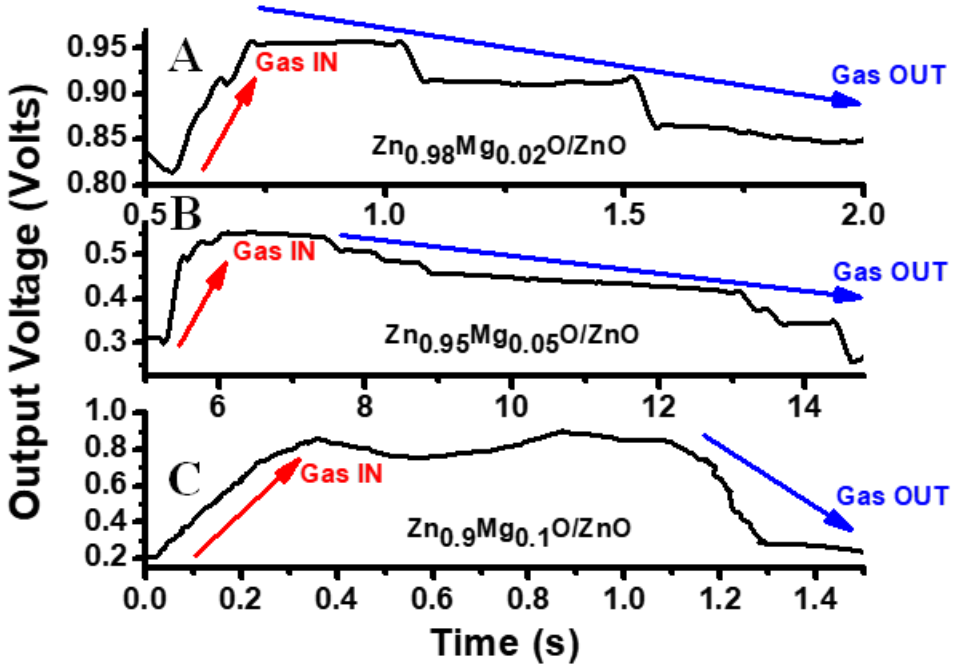

Fig. 4.5: Shows the variation on voltage through the load resistance of the methanol sensors as gas get introduced on chamber. Prior introducing methanol gas to the chamber, the flow rate is stabilized to a concentration of approximately 5,000ppm. Once the gas is introduced, the variation in resistance is measured, followed by vent of the gas, exposing the sensor to dry air.

Native defects at the surface of metal oxides have been theoretically predicted to dominate the chemical properties and adsorption behavior [12]. The photoluminescence (PL) spectra for different Mg mole fraction core-shell structures are shown in figure 4.6. The PL was taken at room temperature using a He-Cd 325nm laser line, and the PL spectrum was normalized during calibration at the laser wavelength. Native defects increase as the concentration of Mg at the core increases with the sensitivity increasing proportionately for high concentration of methanol (> 5000ppm), 25%, 48% and 50% (CS-0.02, CS-0.05 and CS-0.10, respectively). For example, the maxima for the peak at 440nm (shallow donor oxygen vacancy transition [13]) are 0.3852mV, 0.4558mV and 0.84mV for CS-0.02, CS-0.05 and CS-0.10, respectively. The intensity of the PL spectra increases almost linearly with increasing Mg concentration while the sensitivity increased at a sub-linear rate with Mg mole fraction. This observation is in agreement with direct correlation of native defects in ZnO NWs and associated higher sensitivity in gas sensing reported by Ahn et al. [14] The native defects along with their intensity becoming increasingly more prominent with increasing Mg mole fraction in a core-shell structure may be correlated with either : a) increase in strain as the lattice mismatch between ZnMgO/ZnO at the heterointerface increases with larger Mg concentration, b) or dislocations at the interface that increase with shell thickness. As the thickness of the shell approximate to the critical layer thickness (h_c) for larger Mg mole fraction (h_c for $Zn_{0.98}Mg_{0.02}O$/ZnO = 117nm, hc for

$Zn_{0.95}Mg_{0.05}O/ZnO$ = 56nm and h_c for $Zn_{0.9}Mg_{0.1}O/ZnO$ = 55.6nm) the increasing built strain at the interface decrease the formation energy of Vo^{2+}. The formation energy of the point defect decreases with larger Mg mole fraction at the core, therefore, the concentration of point defects increase as shown in equation (2), $c = N_{sites}\, e^{-(E_f/K_b T)}$ where, N_{sites} is the number of sites for the point defect, E_f is the formation energy, k_B is the Boltzmann constant and T is the temperature [15]. If the thickness of the shell exceeds the critical layer thickness, the heteroepitaxial layer relax through dislocations. The enhanced sensitivity observed in core-shell nanostructures may be explained as follows. The native defects of the ZnO nanorods identified in the photoluminescence spectra at room temperature are significantly lower than those for core-shell structures [16]. These defects are attributed to hydrothermal synthesis that typically introduce native defects in ZnO nanorods (the predominant sensing mechanism in ZnO) as compared to other growth techniques [17]. This observation is validated when we compare measured the native defects in $Zn_{0.9}Mg_{0.1}O$ and ZnO nanowires, grown via metal-organic chemical vapor deposition (MOCVD), where no defects in the range of 390nm to 525nm are observed (see figure B). Therefore, the high density of native defects observed in core-shell structures is not due only to hydrothermal growth but may have been introduced either by strain developed at the ZnMgO/ZnO heterointerface that increase with increasing Mg mole fraction at the core or interface states. Similar increment in native defects in a core-shell structure was observed for CdSe/CdS using steady state PL and time-domain PL [18]. Chen et al. observed that upon passivation CdS shell of few monolayers was able to remove surface defects with improved PL that otherwise were plagued by strain induced native defects. In addition to introducing

defects, MgO in ZnO improve the dissociation of methanol to CH_3O^- and H^+ contributing to higher sensitivity [19].

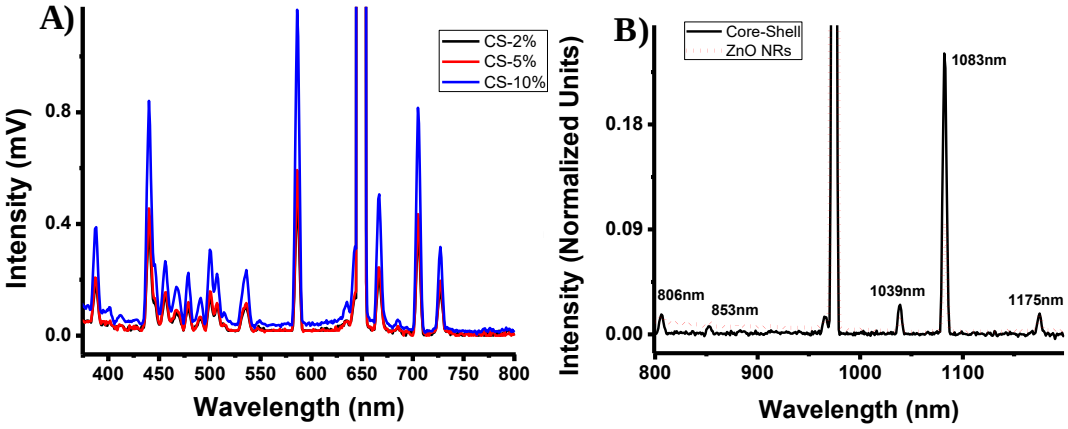

Fig. 4.6: A) Shows the photoluminescence (PL) spectrum of the CS structure for different Mg mole fractions. B) Shows the PL for ZnO NRs and $Zn_{0.9}Mg_{0.1}O$ NWs with a minimum of native defects, in contrast to CS structures.

4.4 Conclusions

Co-axial $Zn_{1-x}Mg_xO$ core, ZnO shell structure were consistently grown using MOCVD with Mg mole fractions of 2, 5 and 10%. The variation of Mg mole fraction at the core was achieved by adjusting the Cp_2Mg/DEZn ratio and tuning the annealing conditions. The coaxial core shell structure and the Mg mole fraction at the core was confirmed using SEM equipped with EDS, high resolution TEM (also equipped with EDS) and XRD. In the case of bright field TEM images, a brightness contrast was observed between the core and the shell. An overlapping in the diffraction peaks was observed with XRD measurements associated to ZnO (002). After being decomposed using a Lorentzian fit, the peaks corresponding to ZnO and ZnMgO were identified, confirming the observations from SEM and TEM. The adsorption and desorption properties of the CS were explored under

methanol atmosphere. The energy trap for CS-0.02, CS-0.05 and CS-0.1 corresponds to doubly charged oxygen vacancy (V_o^{2+}). The sensitivity of the devices were also measured at room temperature showing an increase with the increment of Mg mole fraction at the core for high concentration of methanol attributed to larger defect at the ZnMgO/ZnO interface.

References:

1. P. Shimpi, Y. Ding, E. Suarez, J. Ayers, P-X Gao, Appl. Phys. Lett. 97 (2010) 103104
2. A. Ohtomo, M. Kawasaki, T. Koida, K. Masubuchi, H. Koinuma, Y. Sakurai, Y. Yoshida, T. Yasuda, Y. Segawa, Appl. Phys. Lett. 72, (1998) 2466
3. V-S. Chang, C-T. Chien, C-W. Chen, T-Y. Chu, H-H. Chiang, C-H. Ku, J-J. Wu, C-S. Lin, LC. Chen, K-H. Chen, J. Appl. Phys. 101 (2007) 033502
4. M. Zhi, Z. Zhu, Z. Ye, F. Wang, B. Zhao, J. Phys. Chem. B Vol 109, (2005) 23930
5. T.A. Wassner, B. Laumer, S. Maier, A. Laufer, B.K. Meyer, M. Stutzman, M. Eickhoff, J. Appl. Phys. 106 (2009) 051111
6. M. Bowker, H. Houghton and K.C. Waugh, J. Chem. Soc., Faraday Trans. 1, 1981, 77, 3023-3036
7. Q. Gao, W-T. Zheng, C-D Wei, H-W. Lin, Journal of Nanomaterials Vol 2013 Article ID 263852
8. S. Tian, F. Yang, D. Zeng, C. Xie, J. Phys. Chem. C. 116 (2012) 10586-10591
9. S.S. Islam, A.F.M. Anwar, and R.T. Webster, IEEE TRANSACTIONS ON ELECTRON DEVICES, 51 (2004) 846-853
10. G, Chicot, P. Muret, J.-L. Santailler, G. Feullet, J. Pernot, J. Phys. D: Appl. Phys. 47 (2014) 465103

11. A.B. Djurisic, A.M.C. Ng, X.Y. Chen, Progress in Quantum Electronics 34 (2010) 191-259
12. M.W. Ahn, K.S. Park, J.H. Heo, J.H. Park, et al. Appl. Phys. Lett. 93 (2008) 263103, Nanotechnology 17 (2006) 3012-3017
13. A.B. Djurisic, A.M.C. Ng, X.Y. Chen, Progress in Quantum Electronics 34 (2010) 191-259
14. M.W. Ahn, K.S. Park, J.H. Heo, J.H. Park, et al. Appl. Phys. Lett. 93 (2008) 263103, Nanotechnology 17 (2006) 3012-3017
15. A. Janotti, C.G. Van de Walle, Phys. Rev. B 76 (2007) 165202
16. A. Rivera, A. Mazady, M. Anwar Solid State Electronics 104 (2015) 126-130
17. Hsu et al., Appl. Phys. Lett 92 (2008) 133507
18. X. Chen, Y. Lou, A.C. Samia, C. Burda, Nano Letters 3 (2003) 799-803
19. H.V. Lee, Y.H. Taufiq-Yap, M.Z. Hussein and R. Yunus, Energy 49 (2013) 12-18

Chapter 5

Horizontal ZnO Nanorods

This chapter presents the growth dynamics of ZnO horizontal nanorods without pre-treating the substrate using patterns, etching or catalyst. The ratio of the $Zn^{2+}$and OH^- ions contributes to whether the nanorods will be oriented along the (002) or (001) plane. Additionally, the physical and crystal properties of the horizontal nanorods are presented.

5.1 Growth ZnO horizontal nanorods.

ZnO horizontal nanorods were grown on ZnO thin film/p-Si, as described in section 2.1. The samples are immersed in an aqueous solution upside down at the surface of the solution. The solutions have: 10 mL of DI (deionized) water, with 27mMol of hexamethylenetetramine (HMTA) and different concentration of zinc nitrate hexahydrate ($Zn(NO_3)_2 + 6H_2O$), 3.29mMol, 6.53mMol, 11.35mMol and 17mMol. The glass bottles are placed in a water bath at 90º C during a period of 6 – 20 hours.

5.2 Discussion

Figure 5.1-(A, B) shows environmental scanning electron micrographs (E-SEM) of NRs grown on ZnO thin film. The horizontal nanorods had a length and diameter distribution of 1 – 7μm and 200 – 500nm, respectively, varying depending upon initial precursor ratio (zinc nitrate/HMTA). The lengths and diameters of the NRs also vary with time as the precursor ratio does not remain constant throughout the entire duration of the growth affecting the pH of the solution that in turn modifies the aspect ratio of the

NRs/NWs [1]. The solution containing zinc nitrate and HMTA, acting as zinc and oxygen sources while HMTA acts as a weak base, slowly hydrolyzing in water and releasing OH^-. With time, Zn^{2+} ions would precipitate in the solution changing the pH and altering growth rate. The NRs were grown on ZnO film without pretreatment of the substrates that usually required using metal-catalysts, optical lithography, surface modification via etching or an inhibitor layer. Figure 5.1-C shows the step (or methodology) to achieve quasi-horizontal nanowires [2].

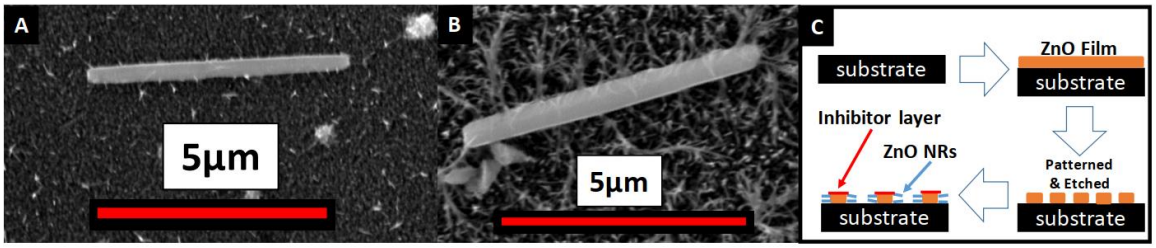

Fig. 5.1: SEM of horizontal NRs grown at 90 °C with a HMTA concentration of 37mg and zinc nitrate of A) 19.4mg, B) 33.7mg. Figure 1-C summarizes typical growth process reported in the literature to achieve "horizontal" NWs/NRs.

Varying the concentration of zinc nitrate ($Zn(NO_3)_2$) while keeping HMTA constant resulted indifferent horizontal NRs density. Density of horizontal NRs increased with lower zinc nitrate concentration for the same growth time, 18hrs. The table 5.1 summarized the growth conditions, showing three $Zn(NO_3)_2$ concentrations of 3.29mMol, 6.53mMol and 11.35mMol, keeping HMTA concentration constant at 27mMol and the volume of de-ionized (DI) water fixed at 10 mL. The amount of Zn ions is proportional to the concentration of Zinc Nitrate in the solution. Note that Zn^{+2} ions are the limiting reagent, while OH^- ions are the excess reagent. Figure 5.2 show that the density of horizontal nanorods decreases (from left to right) for increasing concentration of zinc nitrate, an

observation supported by Ye Sun et al. [3]. By increasing the amount of Zn^{+2} ions, less horizontal nanorods are observed and small nanowires begin to grow. In sample number 4 with zinc nitrate concentration of 50.8mg, few horizontal nanorods are observed with a uniform distribution of nano-strings under the NRs. The supersaturation degree of the solution, for prolonged duration of growth, promotes the growth of vertical nanowires instead.

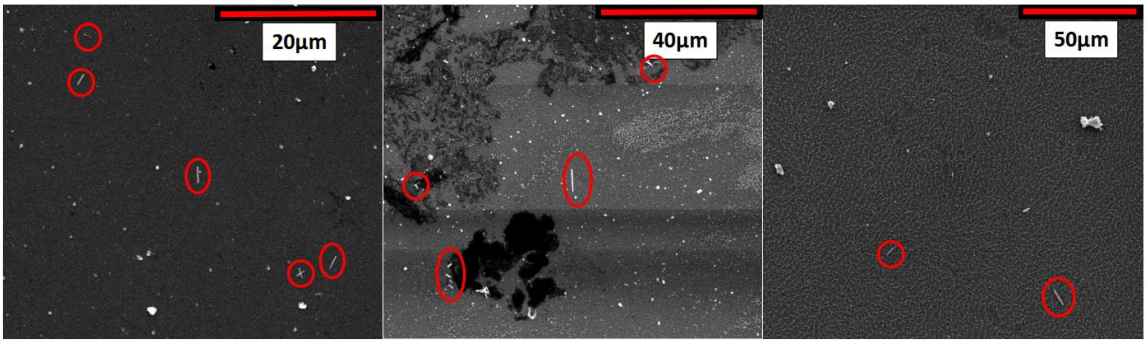

Fig. 5.2: SEM of horizontal nanorods grown using hydrothermal synthesis. The left-image shows 6 NRs on a 48µm x 48µm area for a zinc nitrate concentration of 9.8mg. The center-image shows 8 NRs on a 88µm x 88µm area for a zinc nitrate concentration of 19.4mg. The right-image shows 3 NRs on a 170µm x 170µm area for a zinc nitrate concentration of 33.7mg.

For a $Zn(NO_3)_2$ concentration between 3.29mMol and 11.35mMol, the NRs are symmetrical along the vertical axis and the diameters slightly decrease at the tips of the NRs forming nano-dumbells [4]. In the case of Zn^{2+} concentration of 3.29 mMol or lower, an asymmetric growth along the vertical axis was observed as shown in figure 5.3. The asymmetric formation takes place when the growth along (0001) reaches an equilibrium and the growth along (0001) direction is favored instead. With the samples exposed to the solution for a prolonged period of time, concentration of Zn^{2+} ions become low and ZnO

facet with negatively charged oxygen termination (0001) is favored at this stage [5-6]. The growth kinetics along (0001) may be reduced by increasing zinc nitrate concentration from 9.8 mg to 19.4mg. With increased concentration of zinc nitrate the NWs become oxygen deficient, as is observed from energy dispersive X-ray spectroscopy (EDS) measurements, resulting in slower growth rate along (0001). For example, EDS shows a Zn:O ratio of 0.90:1 in sample number 1 (9.8mg of zinc nitrate), Zn:O ratio of 0.98:1 for sample 2 (19.4mg of zinc nitrate), Zn:O ratio of 1:0.79 for sample 3 (33.7mg of zinc nitrate) and, Zn:O ratio of 1:0.75 for sample 4 (50.3mg of zinc nitrate).

Table 5.1: Summary of growth for ZnO horizontal nanorods grown at 90 °C using hydrothermal synthesis for 18hrs

Zinc Nitrate	HMTA	Approx. Ratio Zn:HMTA	Approx. Density
9.8 mg	37.8 mg	1:9	6 NRs on 48x48 µm
19.4 mg	37 mg	1:4	8 NRs on 88x88 µm
33.7 mg	36.6 mg	1:2	3 NRs on 170x170 µm

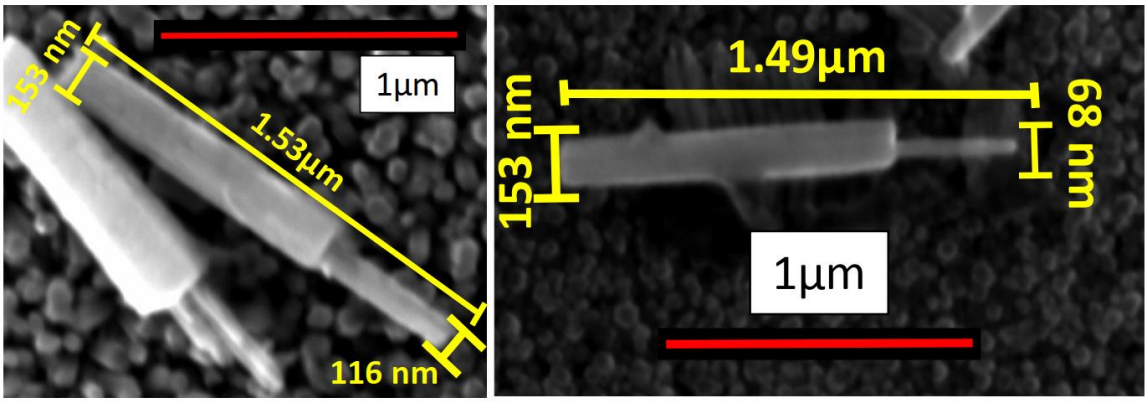

Fig. 5.3: Asymmetrical ZnO horizontal NRs grown with 3.29 mMol of zinc nitrate.

In the present case, the density of the nanorods is determined by the initial precursor ratio, which is easier to control than the previously reported works by other groups. Growth symmetry varied from low to high based upon the initial precursor concentrations. It is to be noted that Qin et al. [2] incorporated Cr layer as an inhibitor to control the density of the nanowires. Soman et al. [8] employed different slit density to control the density of the nanowires. The nanowires demonstrated mirror symmetry along c-axis (vertical axis), but poor symmetry along the horizontal axis. For instance, moving away from the substrate along the vertical axis, the diameter changes from 400nm to 800nm. Similar changes are observed for the lengths of the nanowires varying from 2μm to 8μm.

To further investigate the crystal structure of the horizontal nanorods, the growth was repeated on p-Si substrate without the ZnO buffer layer. The XRD patterns are shown in figure 5.4, with all the peaks corresponding to the silicon substrate except for ZnO (100) at 31.85° (2θ). The a-lattice constant is calculating (from equation 2.2) to be 3.2420 Å. As no other peak corresponding to ZnO is observed, it is appropiate to say that the ZnO nanorods are single crystal. For reference, the XRD for p-Si substrate is shown in Figure 5.4-B.

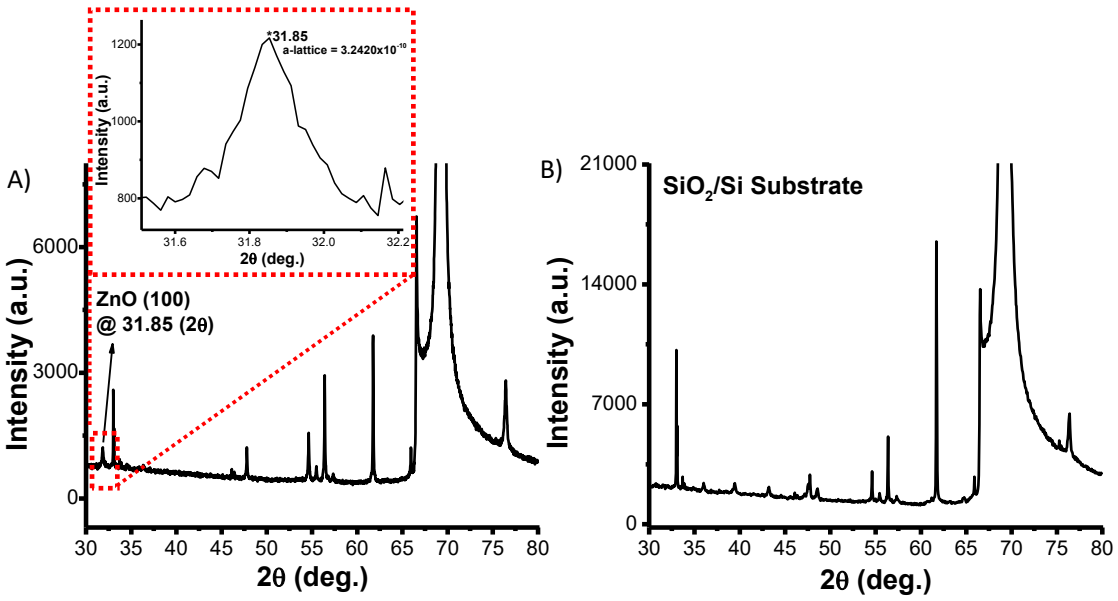

Fig. 5.4: XRD of A) horizontal ZnO nanorods grown on p-Si, with a single diffraction peak at 31.85° (2θ) corresponding to ZnO (100). B) p-Si used as the substrate.

5.3 Conclusions

The growth steps for horizontal nanowires without pre-treatment was developed. The dynamic of the growth was explained in terms of the Zn^{2+} to OH^- ions ratio. The horizontal nanowires had diameters in the range 200 – 500 nm and lengths between 1 – 7 µm, depending upon the growth duration and precursors ratio. Density of horizontal NRs increased with lower zinc nitrate concentration for the same growth time, 18hrs. For a zinc nitrate concentration of 3.29mMol, an asymmetrical growth along the vertical axis was observed possibly due to oxygen termination which resulted in slower growth rate along (0001). These observations were validated using EDS which reflected higher concentration of oxygen in the ZnO NRs prepared with lower concentration zinc nitrate. XRD also confirmed that the NRs are single crystal oriented in the (001) plane or parallel to the substrate.

References:

1. P. Shimpi, Y. Ding, E. Suarez, J. Ayers, P-X Gao, Appl. Phys. Lett. 97 (2010) 103104
2. J. Song, S. Baek and S. Lim, Physica B. 403 (2008) 1960
3. Y. Qin, R. Yang, and Z.L. Wang, J. Phys. Chem. C. Vol. 112 No. 48, (2008) 18734
4. Y. Sun, N.A. Fox, D.J. Riley and M.N.R. Ashfold, Phys. Chem. C, 112, (2008) 9234-9239
5. W. Zhao, X. Song, G. Chen, and S. Sun, Cryst. Res. Technol. 44, No. 4, (2009) 373
6. Z.L. Wang, X.Y. Kong, and J.M. Zuo, Phys. Rev. Lett. 91 (2003), 185502
7. J. Xia X-H. Lu, C-S. Wang, Y-X. Tong and L-P Chen, J. Electrochem. Soc., 158 (2011) D244-D247
8. P. Soman, M. Darnell, M.D. Feldman and S. Chen, J. Nanoscience and Nanotechnology 11, (2011) 1-6

Chapter 6

ZnMgO/ZnO HFET

This chapter describes the fabrication and performance of the back gate ZnO FET. The device, as reported previously, requires a large positive gate voltage to turn the device on, while the current density remains relatively low when compared to Si-based devices. Nevertheless, a ZnMgO/ZnO heteroepitaxial layer used as the active channel could improve the device performance by at least $1x10^3$ mA/mm as demonstrated.

6.1 ZnO Back Gate FET

6.1.1 Fabrication ZnO Back Gate FET

p-Si substrate was cleaned under ultrasound on acetone and methanol. Then rinsed in DI water and dried at 150°C for 15min. The ZnO film was fabricated using the MOCVD, at 300°C for 6min 35sec, using 50sccm of DEZn @20°C and a bubbler pressure of 300 Torrs while flowing 102sccm of N_2 through injector 2. N_2O was used as the oxygen source with 35sccm and 0.65SLPM of N_2 in the background. Then, the ZnO film was annealed at 625°C for 10 min under 1 SLPM of N_2 in the background.

After the growth of the film, the sample was cleaned under ultrasound on acetone and methanol as described previously. Positive photoresist S1805 was span coated at 4000 rpm for 1 min, followed by soft-bake for 1 min at 100°C (115°C in the hot plate). Then the sample was exposed to UV for 5 sec and developed using MF-CD-26 developer. The source and drain were deposited using plasma gold sputtering for 120 seconds two times.

The same process was used for the back gate. Finally, the sample was annealed for 1 min 30 sec at 150°C in an oven. The structure is shown in Fig 6.1

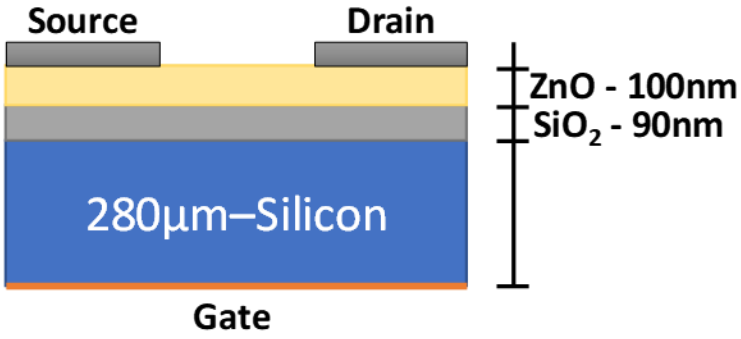

Fig. 6.1: Schematic of the ZnO thin film back gate transistor.

6.1.2 ZnO FET Back Gate Device Performance

The drain current vs. drain voltage for different gate voltages is shown in Fig 6.2. The device exhibits a drain current in the order of few microamps with a threshold voltage of about 5 V. The device has a width of 76µm, while the length is of 19µm, resulting in a W/L ratio of 4. The effective low field mobility ($\mu_{n\text{-}eff}$) is estimated to be 0.1 $cm^2/V.s$ at I_D = 1.66µA for a V_{GS} = 20 V, V_T = 5V, k_n' = $3.33x10^{-9}$ A/V^2 and C_{ox} = $3.64x10^{-4}$ F/m^2. The performance of the ZnO FET is similar to those reported previously, with the exception that those devices have a larger W/L when compare to 4. For example, Cross et. al. reported a ZnO thin film transistor with a thickness of 150 nm grown via RF sputtering, with a W/L ratio of 20 yielding to an effective mobility of 0.8 – 2.3 $cm^2/V.s$ with a threshold voltage of 15 V [**1**]. Similarly, R.L. Hoffman, reported a 50 nm ZnO thin FET using a back gate with a W/L 9:1, resulting in $\mu_{n\text{-}eff}$ = 25 $cm^2/V.s$ at a gate/source voltage of about 60 V [2].

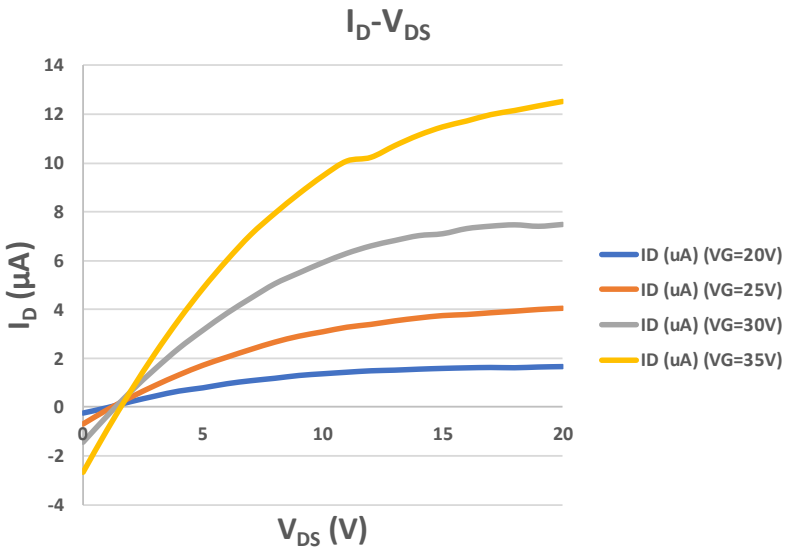

Fig. 6.2: I_D – V_{DS} characteristics for a ZnO thin FET with a V_{GS} = 20 – 35 V.

6.2 ZnMgO/ZnO Heterojunction Back Gate FET

6.2.1 Fabrication ZnMgO/ZnO Heterojunction Back Gate FET

The fabrication of the ZnMgO/ZnO HFET followed the same steps as for the ZnO FET described in section 6.1.1, with the addition of the ZnMgO thin film layer. ZnMgO was grown at 300° C for 1 minute, using 50 sccm of DEZn and 200 sccm of Cp_2Mg (zinc and magnesium precursors, respectively). Afterwards, the ZnMgO layer was annealed at 800°C for 10 minutes under N_2. Fig 6.3 shows a schematic of the fabricated device. The fabrication steps have been summarized in Fig 6.4, similar to the ZnO FET, with the addition that the metal contacts were annealed at 300C for 1 min under N_2.

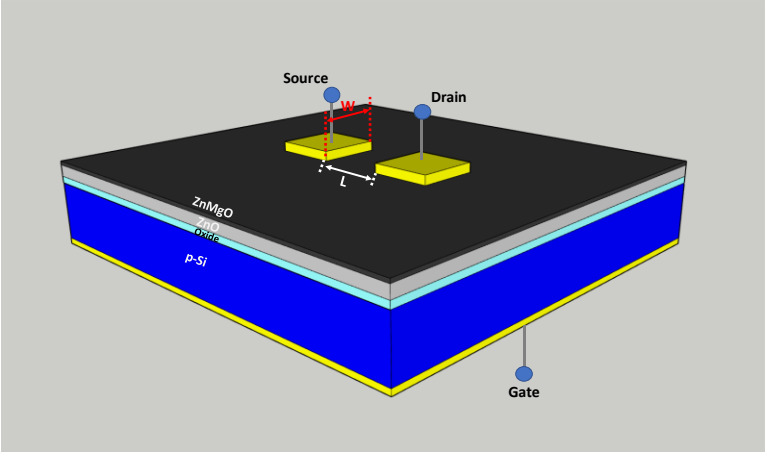

Fig. 6.3: Schematic of the ZnMgO/ZnO thin film back gate transistor.

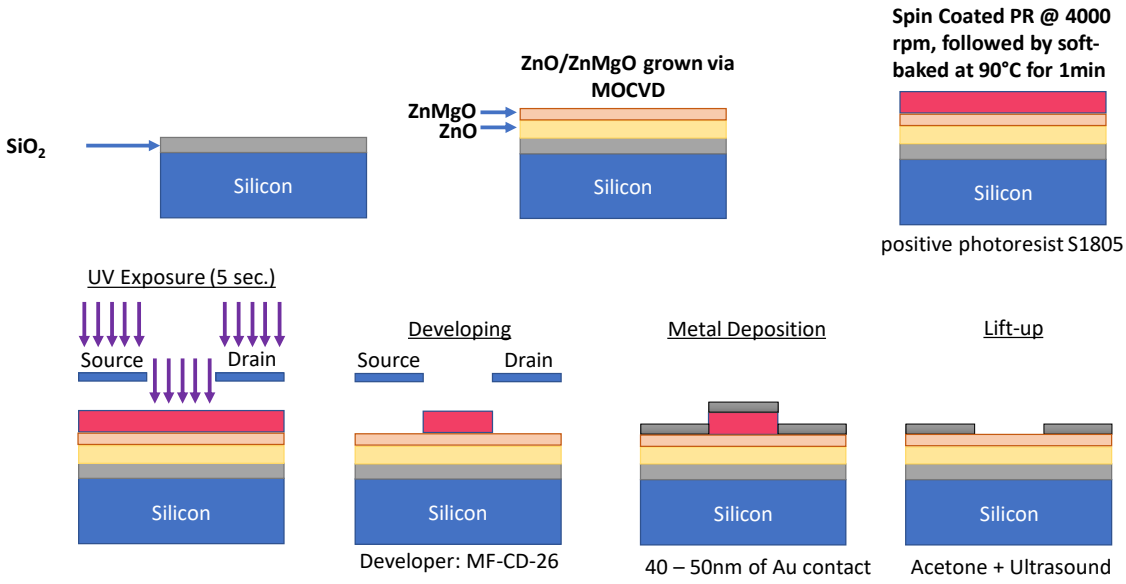

Fig. 6.4: Fabrication steps for the ZnMgO/ZnO thin film back gate transistor.

6.2.2 ZnMgO/ZnO Heterojunction Back Gate FET Device Performance

The dc performance of the ZnMgO/ZnO back gate HFET shows an I_{DS} of about 1.5 mA/mm (~ 0.1 mA) for a V_{GS} = 40 V, as shown in Fig 6.5. The HFET structure resulted in a drain current $1x10^5$ times larger as compared to the same device with only ZnO active

layer. An improvement in the drain current could be as a consequence of a 2-DEG concentration, however, still needs to be further investigate. The 2-DEG formation in ZnO/ZnMgO, relies on electron confinement at the interface due to the conduction band offset and polar surface [3]. The large gate potential applied between terminal source and gate could be imposed by the thickness of the p-Si substrate (230μ), which may be avoided by rather using a top gate, see next section. A maximum transconductance of 0.15 mS/mm was observed. No ZnMgO/ZnO HFET back gate device has been reported before.

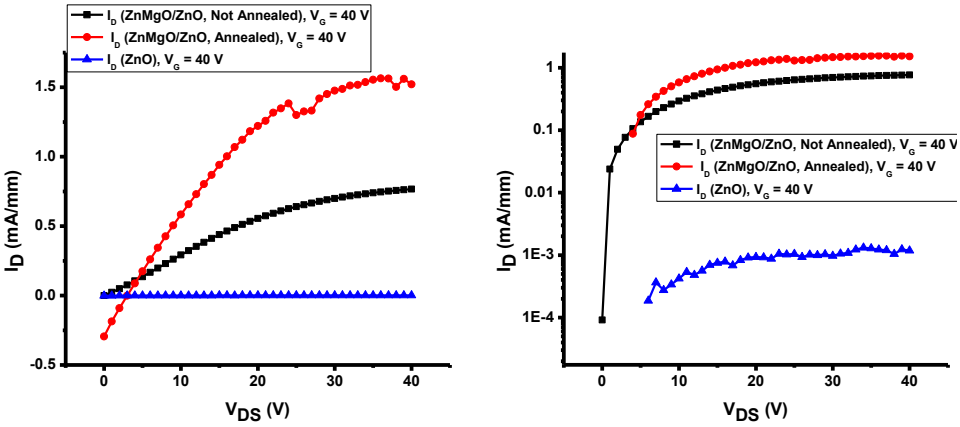

Fig. 6.5: Drain current vs drain voltage, comparing the performances of the ZnMgO/ZnO and ZnO based devices. The right-hand I-V characteristics is shown in logarithmic scale.

6.3 Future Recommendations

The outstanding quality of the ZnO film has been demonstrated by the FWHM of the XRD data, the low native defects in the room temperature PL, as seen in chapter 2, and the electron mobility of 531 $cm^2/V.s$. The quality of the ZnO surpass GaN, which typically has large defect density and lower saturation velocity ($3x10^7$ cm/s at an electric field of 175 kV/cm, and $3.25x10^7$ cm/s at an electric field of 260 kV/cm, for GaN and ZnO, respectively [4]. Nevertheless, there is room for improvement when it comes to design and fabrication of the HFET structures. Perhaps, a top gate contact that would reduce the applied gate bias.

The suggested design and fabrication steps are illustrated in fig 6.6 and 6.7, respectively. In addition, characterization of the ZnMgO/ZnO interface using SIMS (secondary ion mass spectroscopy) to confirm the 2-DEG concentration is required. Specifically, to characterizes the 2-DEG concentration as function of Mg mole fraction and thickness of the ZnMgO layer.

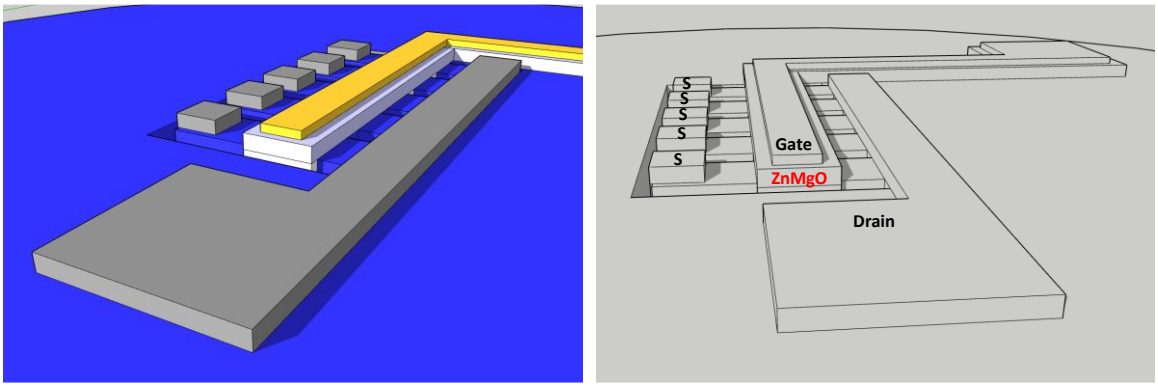

Fig. 6.6: Schematic of design for ZnMgO/ZnO HFET

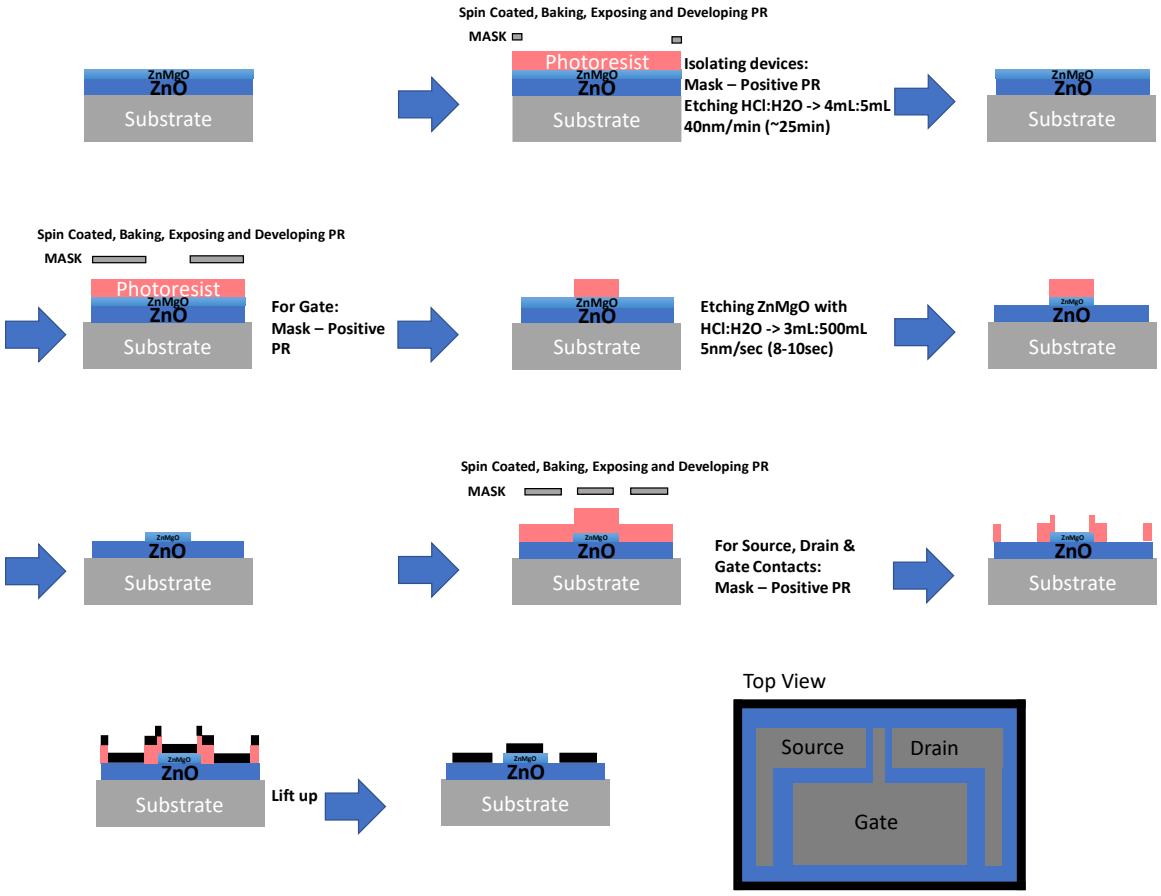

Fig. 6.7: Design, fabrication steps for the ZnMgO/ZnO HFET.

References

1 R.B.M. Cross, M.M. De Souze, Appl. Phys. Lett. 89, 263513 (2006)

2 R.L. Hoffman, J. Appl. Phys. 95, 5813 (2004)

3 H. Faber, S. Das, Y.-H. Lin, N. Pliatsikas, K. Zhao, T. Kehagias, et. al. Science Advances 3, e1602640, 2017

4 Morkoç, H., & Özgür, U. (2009). Zinc oxide: Fundamentals, materials and device technology. Weinheim: Wiley-VCH.